

Manuscript Number:

Title: Effects of episodic methane seepage on the formation and geochemical composition of authigenic minerals: the case of Paola Ridge (southern Tyrrhenian Sea)

Article Type: Full Length Article

Keywords: methane seepage; methanogenesis; authigenic carbonates; authigenic siderite; rare earth elements; REE; stable isotopes

Corresponding Author: Dr. Fulvio Franchi, Ph.D.

Corresponding Author's Institution: BIUST

First Author: Fulvio Franchi, Ph.D.

Order of Authors: Fulvio Franchi, Ph.D.; Marzia Rovere, PhD; Fabiano Gamberi, PhD; Heba Rashed, MSc; Orlando Vaselli, PhD; Franco Tassi, PhD

Abstract: Concretions of authigenic minerals formed in shallow sub-bottom sediments of the Paola Ridge (southern Tyrrhenian Sea) were investigated for their geochemical and isotopic composition. These concretions were collected in an area characterized by the presence of two alleged mud volcanoes and two mud diapirs. The mud diapirs are dotted by pockmarks and dissected by normal faults, and are known for having been a site of fluid seepage for at least the past 40 kyrs. Present-day venting activity occurs alongside the two alleged mud volcanoes and is dominated by CO₂-rich discharging fluids.

In this study, we used stable isotopes (carbon and oxygen) of carbonates coupled with rare earth element (REE) composition of different carbonate and non-carbonate phases for tracing fluid composition and early diagenesis of authigenic precipitates. The analyses on authigenic precipitates are coupled with chemical investigation of venting gas and sea-water.

Authigenic calcite/aragonite concretions, from surficial sediments on diapiric structures, have depleted ¹³C isotopic composition and slightly positive $\delta^{18}\text{O}$ values. By contrast, siderite concretions, generally found within the first 6 m of sediments on the alleged mud volcanoes, yielded positive $\delta^{13}\text{C}$ and $\delta^{18}\text{O}$ values. A flat REE pattern and absence of Ce anomaly in the calcite/aragonite concretions suggests that the methane flux was likely discontinuous and the shallow sub-bottom sediments were affected by downward migration of sea-water. The siderite REE pattern shows consistent LREE (light REE) fractionation, MREE (medium REE) enrichment and positive Gd and La anomalies, suggesting formation close to the exchange equilibrium of adsorbed/dissolved REE under prolonged reducing conditions close to the Fe-reducing zone.

As shown by the REE distribution, the ¹³C-depleted composition and their association with chemosymbiotic fauna, calcite/aragonite precipitated at time of moderate to high methane flux close to the seafloor, under the influence of bottom seawater. Authigenic siderite, on the other hand, formed in the subseafloor, during periods of lower gas discharges under prolonged anoxic conditions within sediments in equilibrium with ¹³C-rich

dissolved inorganic carbon (DIC) from organic matter fermentation and ^{18}O -rich water, likely related to methanogenesis and intermittent venting of deep-sourced CO_2 .

Suggested Reviewers: Vitor Hugo Magalhaes PhD
Universidade de Aveiro
vhm@ua.pt
Expert in authigenic carbonates, stable isotopes of C and O, marine geology in the Mediterranean Sea

Rossella Capozzi PhD
Ass. Prof, BiGeA, University of Bologna
rossella.capozzi@unibo.it
Fluid migration and natural leakage of brines and hydrocarbon (oil, gas and condensate), locally occurring in association with mud volcanoes, and relationships with fluid geochemistry, stratigraphic and tectonic setting in the northern Apennines, Adriatic Sea, Calabrian Arc, etc.

Eric Otto Walliser PhD
University of Mainz
walliser@uni-mainz.de
Authigenic carbonates, methane seepage through burrows in recent and ancient sediments, marine geology and geochemistry, paleogeography and palaeoecology, bivalves and chemosymbiotic bivalves

Daniel Birgel PhD
University of Hamburg
daniel.birgel@uni-hamburg.de
Dr Birgel is one of the leading expert in the study of authigenic carbonates, methane seepage and carbonate geochemistry.

Silvia Ceramicola PhD
Istituto Nazionale di Oceanografia e di Geofisica Sperimentale
sceramicola@ogs.trieste.it
Dr Ceramicola is an experienced marine geologist. She published studies on mud volcanoes and fluid venting. She contributed to the discovery of a new mud volcano province in relation to the Calabrian accretionary wedge in the Ionian Sea.

Stefano Bernasconi PhD
ETH
stefano.bernasconi@erdw.ethz.ch
Stefano Bernasconi's research focuses on the study of biogeochemical processes in terrestrial and marine environments. He has strongly promoted interdisciplinary research at the interface between geology and biology. He is an expert in stable isotopes and organic geochemistry.

Rosalie Tostevin PhD
University of Oxford
rosalie.tostevin@earth.ox.ac.uk
Dr Tostevin main field of research is chemical sedimentology: biotic processes and geomicrobiology; Rare earth elements and use of Ce anomaly in carbonate; cycle of sulfur in marine environment; redox conditions and anoxia.

To: M. Zecchin, Editor in Chief Marine and Petroleum Geology

Manuscript submission

Palapye, 6 March 2017

Dear Editor,

Please find attached a manuscript by F. Franchi and Co-Authors entitled **“Effects of episodic methane seepage on the formation and geochemical composition of authigenic minerals: the case of Paola Ridge (southern Tyrrhenian Sea)”** which I submit to Marine and Petroleum Geology. The manuscript includes a main text, 8 tables and 10 figures. We also arranged a table as supplementary material.

This manuscript describes the process of methane seepage along Paola Ridge in the Southern Tyrrhenian Sea tracing the provenance and composition of mineralizing fluids and outlining their interaction with shallow marine sediments.

In this paper we propose a comprehensive geochemical data set coupled with detailed sedimentological observations of the different carbonate concretions coupled with chemical characterization of seeping gases and bottom seawater. Calcite/aragonite, siderite, sulfide and oxyhydroxide concretions have been investigated for their trace and rare earth elements (REE) distribution, and carbonates have been investigated for their stable isotopes composition (C and O).

This manuscript gives new insights on the past and active processes along the Paola Ridge providing new constrains for the genesis of different authigenic phases. Our data set sheds light onto a composite scenario unraveling the effects of discontinuous methane seepage on the geochemical composition of shallow marine sediments.

We believe that the understanding of such interactions is important for the improvement of our knowledge of environmental conditions and geochemical variability of cold seeps. Furthermore, we provide here new insights into the behavior of REE and other redox sensitive trace elements (i.e. Mo and U) within recent marine sediments providing new tools for marine and sedimentological research.

This research was supported by the flagship project Ritmare (www.ritmare.it) funded by the Italian Ministry of Research and Education (MIUR).

Sincerely,

Fulvio Franchi
Department of Earth and Environmental Sciences, BIUST
Plot 10071, Palapye, BOTSWANA
franchif@biust.ac.bw
Mobile: +267 74531017
Office: +267 4931549

HIGHLIGHTS

- We investigated geochemical composition of authigenic minerals from Paola Ridge
- We investigated chemical composition of bottom seawater and venting gases
- Variation in seepage activity induces formation of different authigenic minerals
- Calcite/aragonite concretions precipitates during moderate to high methane flux
- Siderite forms during low methane flux below the sulfate-methane transition zone

1
2
3
4
5
6
7
8
9
10
11
12
13
14
15
16
17
18
19
20
21
22
23
24
25
26
27
28
29
30
31
32
33
34
35
36
37
38
39
40
41
42
43
44
45
46
47
48
49
50
51
52
53
54
55
56
57
58
59
60
61
62
63
64
65

Effects of episodic methane seepage on the formation and geochemical composition of authigenic minerals: the case of Paola Ridge (southern Tyrrhenian Sea)

Franchi, F.^{1,2}, Rovere, M.², Gamberi, F.², Rashed, H.³, Vaselli, O.^{3,4}, Tassi, F.^{3,4}

1. Department of Earth and Environmental Science, BIUST, Private Bag 16, Plot 10071, Palapye, BOTSWANA

2. ISMAR-CNR, U.O.S. Bologna, via Gobetti 101, 40129 Bologna, ITALY

3. Department of Earth Sciences, University of Florence, Via G. La Pira, 4, 50121 Florence, ITALY

4. IGG-CNR, U.O.S. Florence, Via G. La Pira, 4, 50121 Florence, ITALY

ABSTRACT

Concretions of authigenic minerals formed in shallow sub-bottom sediments of the Paola Ridge (southern Tyrrhenian Sea) were investigated for their geochemical and isotopic composition. These concretions were collected in an area characterized by the presence of two alleged mud volcanoes and two mud diapirs. The mud diapirs are dotted by pockmarks and dissected by normal faults, and are known for having been a site of fluid seepage for at least the past 40 kyrs. Present-day venting activity occurs alongside the two alleged mud volcanoes and is dominated by CO₂-rich discharging fluids.

In this study, we used stable isotopes (carbon and oxygen) of carbonates coupled with rare earth element (REE) composition of different carbonate and non-carbonate phases for tracing fluid composition and early diagenesis of authigenic precipitates. The analyses on authigenic precipitates are coupled with chemical investigation of venting gas and sea-water.

1 Authigenic calcite/aragonite concretions, from surficial sediments on diapiric struc-
2 tures, have depleted ^{13}C isotopic composition and slightly positive $\delta^{18}\text{O}$ values. By contrast,
3
4 siderite concretions, generally found within the first 6 m of sediments on the alleged mud
5 volcanoes, yielded positive $\delta^{13}\text{C}$ and $\delta^{18}\text{O}$ values. A flat REE pattern and absence of Ce
6
7 anomaly in the calcite/aragonite concretions suggests that the methane flux was likely discon-
8
9 tinuous and the shallow sub-bottom sediments were affected by downward migration of sea-
10 water. The siderite REE pattern shows consistent LREE (light REE) fractionation, MREE
11
12 (medium REE) enrichment and positive Gd and La anomalies, suggesting formation close to
13 the exchange equilibrium of adsorbed/dissolved REE under prolonged reducing conditions
14
15 close to the Fe-reducing zone.
16
17
18
19
20
21
22
23
24

25 As shown by the REE distribution, the ^{13}C -depleted composition and their association
26 with chemosymbiotic fauna, calcite/aragonite precipitated at time of moderate to high me-
27 thane flux close to the seafloor, under the influence of bottom seawater. Authigenic siderite,
28
29 on the other hand, formed in the subseafloor, during periods of lower gas discharges under
30 prolonged anoxic conditions within sediments in equilibrium with ^{13}C -rich dissolved inorgan-
31 ic carbon (DIC) from organic matter fermentation and ^{18}O -rich water, likely related to
32
33 methanogenesis and intermittent venting of deep-sourced CO_2 .
34
35
36
37
38
39
40
41
42
43
44
45

46 **Key words:** methane seepage, methanogenesis, authigenic carbonates, authigenic siderite,
47 rare earth elements, REE, stable isotopes
48
49
50
51
52
53
54
55
56
57
58
59
60
61
62
63
64
65

1. INTRODUCTION

Submarine seepage areas originate from the migration of methane-rich fluids and their discharge at the seafloor through peculiar morphologic features such as mud volcanoes (e.g., Krastel et al., 2003; Løseth et al., 2009), pockmarks (e.g., Hovland et al., 2002; Sultan et al., 2014) and mud diapirs (e.g., Rovere et al., 2014). In such areas, faults may act as plumbing systems, favoring the uprising of fluids from deep-seated sources, which can affect at different degrees the diagenesis of marine sediments (e.g., Hein et al., 2006). The fluids often sustain complex ecosystems with a high degree of biodiversity (e.g., Levin et al., 2016) and significant chemosynthetic biomass, which may drive anaerobic oxidation of methane (AOM) and trigger carbonate mineral precipitation (Boetius and Suess, 2004). In such environments, methane is mostly consumed by sulfate-dependent AOM mediated by microbial consortium (Boetius et al., 2000). The microbial communities release of bicarbonate and hydrogen sulfides. This increases the pore water alkalinity and favors the precipitation of authigenic carbonates. It has been proved that the discontinuous seepage of methane may influence the overall geochemical composition of the authigenic carbonates affecting both stable isotope composition of carbon and oxygen (Birgel et al., 2011; Hu et al., 2014) and the REE distribution (Solomon et al., 2008; Kim et al., 2012; Hu et al., 2014).

The eastern Mediterranean Sea and the eastern part of the central Mediterranean Sea have extensively been investigated for the occurrence of mud volcanism and cold seeps related to the presence of collision zones (Gamberi and Rovere 2010; Ceramicola et al., 2014; Lykousis et al., 2009; Mascle et al., 2014). In the western part of the central Mediterranean Sea, the Tyrrhenian Sea, evidences of fluid seepage are limited to the Adriatic Sea (Geletti et al., 2008), the Strait of Sicily, Sardinian Margin (Della Valle and Gamberi, 2011) and Malta Plateau (Savini et al., 2009; Micallef et al., 2011; Taviani et al., 2013), mostly in the form of

1 pockmarks, occasionally associated with methane-imprinted carbonates (Capozzi et al., 2012;
2 Cangemi et al., 2010; Angeletti et al., 2015; Taviani et al., 2015). In the westernmost part of
3 the Central Mediterranean Sea, the Tyrrhenian Sea, little evidence of past and present fluid
4 circulation has been found, except for the Paola Ridge, along the NW Calabrian margin (Fig.
5 1). This area, surrounded by hydrothermally active vent sites (Peters et al., 2011; Passaro et
6 al., 2016), has been described as a site of intense seepage and gas venting and precipitation of
7 methane-related authigenic carbonates (Gamberi and Rovere, 2010; Rovere et al., 2014,
8 2015).

19
20 Although authigenic calcite and aragonite have commonly been used for geochemical
21 characterization of seeping fluids and paleoenvironmental reconstruction at recent (e.g.,
22 Himmler et al., 2000; Peckmann et al., 2001; Peckmann and Thiel, 2004; Capozzi et al.,
23 2012; Magalhães et al., 2012) and fossil (e.g., Blumemberg et al., 2015; Cau et al., 2015;
24 Viola et al., 2015) methane seeps, the occurrence of authigenic siderite at seepage sites is less
25 documented (Fritz et al., 1971; Curtis et al., 1972; Mozley and Wersin, 1992; Rongemaille et
26 al., 2011). Siderite nodules have been reported in modern settings associated with methane
27 seepage (Niger delta; Rongemaille et al., 2011) or methane hydrate decomposition (Black
28 Outer Ridge; Matsumoto, 1989), and with highly ferruginous, low-sulfate, anoxic lake waters
29 (e.g., Wittkop et al., 2014). Despite the wide occurrence of sedimentary siderite little is
30 known about the chemical conditions in which siderite forms in deep marine settings. Siderite
31 is a common early diagenetic mineral that likely records the chemistry of the mineralizing
32 fluids providing insights into the characteristics of the depositional environments (Mozley
33 and Wersin, 1992). Pioneering studies of deep marine sediments, argued that the isotopic
34 composition of siderite might be the result of the incorporation of deep circulating fluids
35 (Clayton and Epstein, 1961; Muehlenbachs and Hodges, 1978; Cocker et al., 1982).

1 To characterize the pattern of fluid seepage that has triggered the precipitation of
2 authigenic minerals at Paola Ridge, whole rock geochemistry (REE) and stable isotope (car-
3 bon and oxygen) composition were investigated. REE composition of carbonates has success-
4 fully been applied to the reconstruction of seeping fluids composition and redox conditions in
5 both recent (e.g., Himmler et al., 2010; Hu et al., 2014) and ancient (e.g., Nothdurft et al.,
6 2004; Feng et al., 2009; Franchi et al., 2015; 2016) settings. It was proved that a variation of
7 the REE pattern from the standard seawater composition (e.g., Zhong and Mucci, 1995;
8 Zhang and Nozaki, 1998) is related to either mixing processes between methane-rich and hy-
9 drothermal fluids (e.g., Kamber et al., 2004; Feng et al., 2009) or modification of pore water
10 redox conditions (Kim et al., 2012; Hu et al., 2014).
11
12
13
14
15
16
17
18
19
20
21
22
23
24

25 This paper aims at unraveling the dynamic processes occurring in the shallow sub-
26 bottom sediments of Paola Ridge (southern Tyrrhenian Sea) and provides an alternative in-
27 terpretation of peculiar domed morphologies hitherto considered as mud volcanoes (Gamberi
28 and Rovere 2010; Rovere et al., 2014; 2015). By coupling trace elements and REE distribu-
29 tions and the $\delta^{13}\text{C}$ (‰ V-PDB) and $\delta^{18}\text{O}$ (‰ V-PDB) compositions the source of the seeping
30 fluids and redox condition during carbonate precipitation have been pinpointed. This work
31 provides for the first time a detailed genetic scenario consisting of CO_2 venting, intermittent
32 methane seepage and migration of the sulfate-methane transition zone (SMTZ) for the for-
33 mation of authigenic minerals along the Paola Ridge. More broadly, our paper shows that
34 studies combining trace elements and REE analysis have a great potential to shed light on the
35 causes of both siderite precipitation and reconstruction of environmental conditions that can
36 led to a variety of authigenic mineral precipitation.
37
38
39
40
41
42
43
44
45
46
47
48
49
50
51
52
53
54
55
56
57
58
59
60
61
62
63
64
65

2. GEOLOGICAL SETTING

1
2
3
4 The Paola Ridge is a NNW-SSE 60-km-long and ca. 500-m-high anticline that confines
5
6 the Paola Basin westward along the continental slope of the NW Calabrian margin (Fig. 1).
7
8 The Paola Basin lies at the rear of the Calabrian Arc (inset of Fig. 1) in the upper plate of the
9
10 Ionian subducting system (Faccenna et al., 2011). The Paola Basin, along with other basins
11
12 along the Italian margins, originated from the extensional tectonics connected to the southeast
13
14 migration of the Apennine Thrust Belt, this led to the opening of the Tyrrhenian Sea back arc
15
16 basin, (see Milia et al., 2009; Gutscher et al., 2015 and references therein).
17
18
19

20
21 Cold seeps were first identified between 700 and 900 m water depth along the Paola
22
23 Ridge with the aid of full-ocean depth multibeam and backscatter data (Gamberi and Rovere,
24
25 2010). The cold seeps are located on 2 structures initially defined as mud volcanoes (RMV
26
27 and R1MV structures; Gamberi and Rovere 2010; Rovere et al., 2014) and 3 main mud
28
29 diapirs (D1, D2, D3), characterized by the presence of large fields of pockmarks (Fig. 1).
30
31

32
33 Higher resolution geophysical data acquisitions and seafloor sampling campaigns were
34
35 carried out in 2011 and 2014 (Rovere et al., 2014). During these campaigns active gas vent-
36
37 ing at the seafloor, gas plumes in the water column and precipitation of Fe-Mn-oxy-
38
39 hydroxides, sulfide and siderite in the sub-seafloor of the mud volcanoes were detected
40
41 (Rovere et al., 2014; 2015). Authigenic calcite and aragonite concretions were found in the
42
43 shallow subbottom sediments on the mud diapirs. These carbonates are associated with
44
45 chemosymbiotic bivalves, whose radiocarbon indicated ages from a few centuries to at least
46
47 the past 40 kyrs (Rovere et al., 2015).
48
49
50

51
52 All the structures in the area are confined and controlled by normal faults, which repre-
53
54 sent the offshore prolongation of the fault zones dissecting the Calabrian Arc on land and are
55
56 thought to play a key role in driving the fluid seepage, especially in the diapirs D1 and D2
57
58 (Rovere et al., 2014).
59
60
61

3. MATERIALS AND METHODS

Bathymetry, seafloor backscatter and seismic data, gravity- and box-coring samples were acquired in the Paola Ridge area aboard the R/V Urania in 2011 and 2014 (Rovere et al., 2014; 2015). Whole core magnetic susceptibility profiles were obtained by means of a BartingtonTM MS2 meter coupled with a MS2C core-logging sensor at 2 cm spacing.

3.1. Core description

The schematic logs of all the sampled cores are shown in Fig. 2. The sediment cores GC03 and GC17 were sampled at water depths of respectively 550 and 725 m in venting sites of the RMV structure (Fig. 1). GC28 was sampled at a venting site on the R1MV structure. The sediments were deformed and disrupted by gas expansion in the core barrel during the recovering of the coring device. Sulfide and siderite samples were present at different depths (Fig. 2). The sediment cores GC12 (1055 m water depth), GC26 (579 m water depth) and GC29 (707 m water depth) were collected on the R1MV structure (Fig. 1), where gas was apparently trapped 2-3 m below the seafloor. Degassing slowly started when the cored samples were already stored on the deck of the ship, resulting in the formation of expansion cracks (Fig. 2). The core GC12 was collected in the lower slope of the R1MV structure. The cores GC07, GC08 and GC10 were collected on the top of the RMV structure (Fig. 1) and showed features similar to the previously described expansion cracks. They were collected from sites of either slow gas venting or where gas was trapped below the seafloor. The core GC10 was collected at 870 m water depth, in the lower slope of the RMV structure, similarly to GC12, where seismic transparent bodies, interpreted as mudflows, trap the gas a few meters below the seafloor (cf. Rovere et al., 2014). The cores GC15 and GC16 were sampled on the D1 diapir at 520-550 m water depth (Fig. 1). The GC15 core penetrated the sediment

1
2
3
4
5
6
7
8
9
10
11
12
13
14
15
16
17
18
19
20
21
22
23
24
25
26
27
28
29
30
31
32
33
34
35
36
37
38
39
40
41
42
43
44
45
46
47
48
49
50
51
52
53
54
55
56
57
58
59
60
61
62
63
64
65

down to a depth of 4.27 m, whilst the core barrel of GC16 captured some carbonate concretions at the seafloor (Cal-C, Cal-N; Fig. 2). Core GC15 was characterized by intense bioturbation and frequent shell fragments of bivalve mollusks typical of reducing environments, associated with abundant decapod claws (Fig. 2). The cores GC20, GC21 and GC25 were collected between 653 and 694 m water depth across a fault scarp that dissect the D2 diapir (Fig. 1). Core GC20 impacted against a 10-cm-thick aragonite substrate located 1 m below the seafloor. Aragonite was associated with chemosymbiotic bivalves (cf. Rovere et al., 2014; 2015) and abundant remnants of the decapod *Calliax* sp. (Fig. 2). Core GC25 also impacted an aragonite crust, which was located 1 m below the seafloor and associated with chemosymbiotic bivalves. The box core BC25, collected in the same sampling station of core GC25, contained aragonite with vuggy and spongy fabric (Cal-H, Table 1). Core GC21 penetrated in the sediment for 4.4 m. Bioturbation and abundant fragments of chemosymbiotic bivalves were observed throughout the sediment succession. An aragonite crust was found between 2 m and 2.40 m below the seafloor (Fig. 2).

From 16 sampling stations at 16 different sites (Figs. 1-2, Table 1), a total of 32 samples of mud and 37 concretions were collected and analyzed for mineralogical and chemical composition (Tables 2-6). Twenty-one samples are carbonates of different composition: aragonite, calcite, dolomite and siderite (Table 1). For the sake of clarity, the samples were divided into five groups: i) calcite/aragonite concretions (Table 2), ii) siderite concretions (Table 3), iii) sulfide concretions (Table 4), iv) Fe-oxy-hydroxide concretions (Table 5) and v) muddy sediments (Table 6). The petrographic- and microfacies-based analyses were performed using standard petrographic thin sections at Istituto di Scienze Marine-Consiglio Nazionale delle Ricerche (ISMAR-CNR) and Earth and Environmental Science Department at Botswana International University of Science and Technology (BIUST).

3.2. Gas and water samples

1
2 Since strong degassing was noticed once cores were brought to the surface, gases
3 from the discharging vents were collected from the R1MV (MB14_BC05, Fig. 1; Table 7)
4 and the RVM structures (MB14_BC09, Fig. 1; Table 7). The gas samples were then trans-
5 ferred into a 250 mL pre-evacuated glass flask by using a silicon tube inserted into the water
6 vent for major components and $\delta^{13}\text{C-CO}_2$ (see methods in Vaselli et al., 2006).
7
8
9
10

11
12 Five seawater samples (Table 8) were collected at the interface with the sea bottom by
13 means of a rosette sampler alongside R1MV (MB14_ROS5, MB14_ROS6 and
14 MB14_ROS7) and RMV (MB14_ROS8 and MB14_ROS9). Once retrieved at the surface,
15 each water sample was divided into two aliquots and both filtered at 0.45 μm . The first one
16 was transferred to a 125 mL plastic bottle for the determination of the main anions while the
17 second one was acidified with 0.5 mL of suprapur HCl in a 50 mL plastic bottle for the anal-
18 ysis of the main cations. Eventually, a third aliquot was transferred to pre-weighed 100 mL
19 glass bottle, where 5 mL of a 1M Na_2CO_3 solution were previously added, for the determina-
20 tion of free- CO_2 . Sampling procedures followed the protocol described in Cabassi et al.
21 (2011).
22
23
24
25
26
27
28
29
30
31
32
33
34
35
36
37
38

39 **3.3. Analytical procedure**

40
41 Bulk mineralogy was analyzed by X-ray diffraction on powdered samples using a Philips
42 PW 1050/37 diffractometer, with a Cu anode (40 kV accelerating voltage and 20 mA cur-
43 rent), a graphite monochromator and the X'Pert PRO Philips acquisition system (detection
44 limit 4%). The analyses were carried out with a goniometry speed of $20^\circ/\text{min}$, in a scanning
45 range $5-70\ 2\theta^\circ$ for the rock samples and $2-32\ 2\theta^\circ$ for the clay fraction.
46
47
48
49
50
51
52

53
54 Sub-samples for geochemical analyses were powdered using a planetary mill equipped
55 with 4 grinding agate bowls. Major and trace elements (Tables 2-6, supplementary materials
56 S1) were analyzed by X-ray fluorescence (XRF), using a Rigaku II wavelength dispersive
57
58
59
60
61
62
63
64
65

1 spectrometer with a Rh anode on pressed pellets of bulk sample powder, and inductively
2 coupled plasma - mass spectrometry (ICP-MS) at the ACME Laboratories (Canada). Seven
3 additional samples of siderite were analyzed at Activation Laboratories LTD (Canada). In the
4 first set of analyses the powdered samples, weighed (about 0.2 g) in PTFE tubes, were dis-
5 solved with the three-acid (HCl-HF-HNO₃) dissolution method, in a microwave oven. From
6 each sample, an aliquot of approximately 5mL was then transferred to 10 mL tubes and
7 placed in an automatic sampler and analyzed with an Agilent 700 Series ICP-MS. In the se-
8 cond set of analyses (Table 3) the fusion procedure followed the lithium
9 metaborate/tetraborate protocol developed by Activation Laboratories (code 4B and 4B2; see
10 <http://www.actlabs.com/>). Samples were mixed with a flux of lithium metaborate and lithium
11 tetraborate and fused in an induction furnace. The molten melt was immediately poured into a
12 solution of 5% nitric acid containing an internal standard, and mixed continuously until com-
13 pletely dissolved. Each batch of samples contained a method reagent blank, a certified refer-
14 ence material and 17% replicates. The samples were then investigated for their trace elements
15 and REE composition using a Perkin Elmer Sciex ELAN 6000, 6100 or 9000 ICP-MS. Three
16 blanks and five controls (three before each sample group and two after) were analyzed during
17 each batch of samples. Duplicates were fused and analyzed every 15 samples (instrument was
18 recalibrated every 40 samples). Accuracy for trace element determinations was ca. 5% for
19 element concentrations >10 ppm and 10-15% for lower concentrations. Detection limits for
20 XRF and ICP-MS analysis were ca. 3 and 0.1 ppm, respectively.

21
22
23
24
25
26
27
28
29
30
31
32
33
34
35
36
37
38
39
40
41
42
43
44
45
46
47
48
49
50
51
52
53
54
55
56
57
58
59
60
61
62
63
64
65
The relative abundances of REE were normalized to Post Archean Average Australian Shale (PAAS, Taylor and McLennan, 1985), representing the estimated average terrigenous input to the oceanic environment. We calculated Σ REE, Y/Ho, Ce, Eu and Gd anomalies (Tables 2-6) and the relation between these proxies and trace and transition elements for the studied samples. Light REE (LREE) fractionation was calculated as Pr_{SN}/Yb_{SN} to avoid bias

1 due to anomalous La and Ce concentrations. Medium REE (MREE) enrichment was calculat-
2 ed as Gd_{SN}/Yb_{SN} . Normalized Ce, Eu and Gd anomalies were calculated using the geometric
3 equation given by Lawrence et al. (2006):
4
5

$$6 \quad (Ce/Ce^*)_{SN} = Ce_{SN} / [Pr_{SN} * (Pr_{SN} / Nd_{SN})] \quad (1)$$

$$7 \quad (Eu/Eu^*)_{SN} = [Eu_{SN} / [(Sm_{SN})^2 * Tb_{SN}]^{1/3} \quad (2)$$

$$8 \quad Gd/Gd^* = [Gd_{SN} / [(Tb_{SN})^2 * Sm_{SN}]^{1/3} \quad (3)$$

9
10
11
12
13
14
15
16
17
18
19
20
21
22
23
24
25
26
27
28
29
30
31
32
33
34
35
36
37
38
39
40
41
42
43
44
45
46
47
48
49
50
51
52
53
54
55
56
57
58
59
60
61
62
63
64
65
Stable isotopes (C and O) measurements were performed on powdered samples and were
carried out using the Finnigan Delta S mass spectrometer at the Department of Physical and
Geological Sciences of the University of Parma (Italy). Prior the analysis the powdered sam-
ples were ignited under vacuum at 550 °C to remove all organic matter. Then the samples
were transferred to 25 mL flasks equipped with a glass tap and reacted with 4 mL of 100%
anhydrous phosphoric acid at 25 °C after degassing H₃PO₄ under vacuum. The samples were
successively treated for selective acid extraction (see protocol in Al-Aasm et al., 1990). The
results were reported in the conventional δ‰ notation against the V-PDB (Vienna Pee Dee
Belemnite) standard with a reproducibility of ± 0.3‰. Standards used for estimation of exter-
nal precision were Carrara and San Vincenzo marbles (Internal), NBS18 and 327 NBS19 (In-
ternational), whereas the analytical error and the reproducibility were ±0.05‰ and ±0.1‰,
respectively (see Vaselli et al., 2006).

Inorganic low-solubility gases (Table 7) were analyzed by gas-chromatography (GC) us-
ing a Shimadzu 15A equipped with a 10 m long 5A-molecular sieve column and a thermal
conductivity detector (TCD). Methane was analyzed using a Shimadzu 14A gas chromato-
graph equipped with a 10-m-long stainless steel column packed with Chromosorb PAW
80/100 mesh coated with 23% SP 1700 and a flame ionization detector (FID) following the
protocol described in Passaro et al. (2016).

1 The seawater samples (Table 8) were analyzed at the Department of Earth Sciences of the
2 University of Florence by cation- (Na^+ , K^+ , Ca^{2+} , Mg^{2+} , Li^+ , and NH_4^+) and anion- (Cl^- ,
3 SO_4^{2-} , NO_3^- , Br^- and F^-) chromatography by using Metrohm 861 and 761 ion-
4 chromatographers, following the protocol in Cabassi et al. (2011).
5
6
7
8
9

10 11 12 **4. RESULTS**

13 14 15 **4.1. Petrography of the concretions**

16 17 *4.1.1. Calcite/aragonite concretions*

18
19
20
21 Calcite /aragonite concretions, collected from different depths (Table 1), are only
22 found in cores located on D1 and D2 structures (Fig. 2). The concretions are a few centime-
23 ters across, showing variable degree of lithification from poorly cemented to more lithified
24 types (Fig. 3A). These concretions are mainly mudstone/wackestone with foraminifera rem-
25 nants cemented by mottled to homogeneous micrite (Fig. 4A). Patches of sandy limestone
26 were also observed. Porosity is generally low and vugs are filled with sparry calcite and less
27 abundant fibrous cements. The concretions are mainly composed of aragonite with subordi-
28 nate calcite and abundant terrigenous components (Table 1; Fig. 4A). Dolomite occurs as
29 patchy cements within vugs or as millimeter-thick crusts lining the concretions. Two concre-
30 tions (Cal-B and Cal-AA) consist of calcite and dolomite cemented shells of chemosymbiotic
31 bivalves (Table 1; Fig. 2).
32
33
34
35
36
37
38
39
40
41
42
43
44
45
46
47
48

49 50 *4.1.2. Siderite concretions*

51
52 Siderite concretions are only found in cores from the gas venting structures R1MV
53 and RMV (Fig. 2). Siderite crusts and small tubular concretions (Fig. 3B-D) are embedded
54 within the muddy sediments. The tubular concretions are normally a few centimeters long
55 and less than 2 centimeters wide (Fig. 3C-D). In thin section, the concretions display a con-
56
57
58
59
60
61
62
63
64
65

1 centric zonation due to alternating reddish and dark brownish bands (Figs. 3C, 4B). These
2 concretions are made up of dominant siderite with subordinate calcite and terrigenous miner-
3 als (quartz, muscovite, plagioclase, etc.). Most of the concretions consist of microcrystalline
4 siderite, locally showing a clotted fabric. The terrigenous particles are mostly silt-sized and
5 poorly sorted while the clasts of quartz are angular to subrounded. Generally the outer part of
6 the tubular concretion appears turbid with a mottled fabric (Fig. 4B). Thin crusts of sulfides
7 lined the inner part of the tubular concretion (Fig. 4B).
8
9

10
11
12
13
14
15
16
17
18 Two samples of siderite (Cal-FF and Cal-E) are coarse-grained, composed of coarse
19 crystalline siderite with an equigranular hypidiotopic to xenotopic fabric (Fig. 4C).
20
21

22 23 *4.1.3. Sulfide and Fe-Mn-oxy-hydroxide concretions*

24
25
26
27
28
29
30
31
32
33
34
35
36
37
38
39
40
41
42
43
44
45
46
47
48
49
50
51
52
53
54
55
56
57
58
59
60
61
62
63
64
65
Sulfide concretions are dominated by pyrite and marcasite. Concretions of native sul-
fur were also observed (Rovere et al., 2015). They have high porosity and are typically a few
centimeters across (Fig. 5). The sulfide form either isopachous crusts (Fig. 6A) or aggregates
of anhedral and granular pyrite around small and coarse terrigenous clasts (Fig. 6B, C).

The Fe-Mn-oxy-hydroxide concretions are mostly made up of microcrystalline hema-
tite with minor amount of goethite. Terrigenous material was ubiquitous and likely dominant
in the bulk rock.

4.1.4. Muddy sediments

These sediments are vuggy to cohesive, grey to brownish mud and sandy mud. Quartz
is the main component while feldspar (albite and microcline) and other silicates (muscovite,
illite, kaolinite) are subordinate. Mud is mostly deformed, dissected by fractures and locally
present trace of bioturbation (Fig. 2).

4.2. Stable isotopes

The studied carbonates show a relatively wide range of carbon and oxygen isotopic composition (Table 1). The $\delta^{13}\text{C}$ and $\delta^{18}\text{O}$ values of calcite/aragonite concretions varied from -48.8‰ to -26.3‰ V-PDB and from 1.4‰ to 5.5‰ V-PDB, respectively (Table 1). Crusts of dolomite (Cal-B, Cal-C and Cal-N) yielded $\delta^{13}\text{C}$ values ranging between -33.4‰ and -9.9‰ V-PDB. The siderite concretions yielded $\delta^{13}\text{C}$ values ranging between -3.2‰ and 10.6‰ V-PDB while $\delta^{18}\text{O}$ values were comprised between 8.7‰ (Cal-A) to 9.9‰ (Cal-R) V-PDB (Table 1).

The sulfur isotopic compositions of one pyrite concretion and one native sulfur concretion were -32.7‰ and -15.3‰ V-CDT, respectively.

4.3. Major and trace elements

Major element concentrations of calcite/aragonite, siderite, sulfide, Fe-Mn-oxyhydroxide and mud samples are reported in tables 2 to 6 while trace element contents are listed in the supplementary material (S1).

Calcite/aragonite concretions were characterized by high CaO (up to 43.16 wt.%) and relatively high SiO_2 contents (average 16.51 wt.%; Table 2). Iron content (as Fe_2O_3) was generally lower than 5 wt.% within calcite/aragonite concretions (Table 2). Siderite samples showed high Fe contents (between 36.23% and 53.94%) and average SiO_2 contents of 12.21 wt.% (Table 3). Averaged CaO and MgO contents of the siderite concretions were 3.24 wt.% and 1.32 wt.%, respectively (Table 3). The average SiO_2 content in sulfide concretions was about 16.55 wt.% (Table 4), whereas Fe-Mn-oxy-hydroxides showed higher SiO_2 contents (up to 36.12 wt.%). The relatively low MnO contents (average 0.17 wt.%; Table 5) of the Fe-

1 Mn-oxy-hydroxides suggest that the concretions were mainly Fe-oxy-hydroxides. SiO₂ (aver-
2 age 37.66 wt.%), Al₂O₃ (average 14.62 wt.%) and Fe₂O₃ (average 6.97 wt.%) dominated the
3 muddy sediments whilst the CaO average content was 4.95 wt.% (Table 6).
4
5
6

7
8 The distribution of redox-sensitive trace elements, namely U and Mo, has been inves-
9 tigated (Supplementary Materials, S1). Calcite/aragonite concretions show consistent concen-
10 trations of U ranging between 5.3 and 28.5 ppm. The Mo contents in the calcite/aragonite
11 concretions are highly variable with values between 0.9 and 56 ppm. Siderite concretions
12 yielded U values ranging between 0.4 and 13.5 ppm. Even the siderite concretions displayed
13 highly variable Mo concentrations ranging between 1.1 and 84 ppm. Relatively large concen-
14 trations ranges of U and Mo were also showed by sulfide (0.8-12.6 ppm and 11-254.2 ppm,
15 respectively), Fe-oxy-hydroxide (9.2 ppm and 62.7 ppm, respectively) and mud (2.6-13.3
16 ppm and 0.7-77.8 ppm, respectively) samples.
17
18
19
20
21
22
23
24
25
26
27
28
29
30
31
32

33 34 **4.4. REE patterns**

35
36
37 REE concentrations of calcite/aragonite, siderite, sulfides, Fe-oxy-hydroxide concre-
38 tions and muddy sediments are reported in Tables 2 to 6. PAAS-normalized REE patterns are
39 plotted in figures 7 and 8. The average REE patterns within the investigated samples vary
40 according to the different lithotypes.
41
42
43
44
45
46
47

48 Total REE contents in the limestone samples range between 60.7 and 107.6 ppm (Ta-
49 ble 2). Highly variable Σ REE contents were detected in the siderite samples as they range
50 from 33.5 to 153.9 ppm (Table 3). Sulfides and Fe-oxy-hydroxides also showed highly varia-
51 ble Σ REE contents ranging from 18.1 to 132.5 ppm and from 170.9 to 318.0 ppm, respective-
52 ly (Tables 4-5). A general enrichment of REE was recognized in the muddy sediments (Table
53
54
55
56
57
58
59
60
61
62
63
64
65

1 6) with an average value of 237.7 ppm. The calcite/aragonite concretions were characterized
2 by a slight enrichment of LREE compared to HREE (Pr_{SN}/Yb_{SN} between 0.95 and 1.35). No
3
4 Ce and Gd anomalies were detected in the calcite/aragonite samples whilst the Eu anomaly
5
6 was slightly positive (average 1.14). The Y/Ho ratio in the calcite/aragonite (average value of
7
8 29.2, Table 2) approaches the chondritic value (≈ 26 ; e.g., Pack et al., 2007). The average
9
10 LREE/HREE ratio (Pr_{SN}/Yb_{SN}) within the siderite concretions is ca. 0.45 and Ce and Gd
11
12 anomalies are lacking or slightly positive (between 1.00-1.34 and 1.05-1.21, respectively).
13
14 Siderite samples do not show any Eu anomaly. The siderite samples show near-chondritic
15
16 Y/Ho ratios as they vary from 25.6 to 38.4 (Table 3). Sulfide concretions show slight enrich-
17
18 ment of LREE compared to HREE (average $Pr_{SN}/Yb_{SN} = 1.37$). Sulfides show a general lack
19
20 of Ce and Gd as well as Eu anomalies (Table 4). The average Y/Ho value in the sulfide con-
21
22 cretions is about 23.63. The Fe-oxy-hydroxide concretions have a rather flat REE pattern (av-
23
24 erage $Pr_{SN}/Yb_{SN} = 1.1$). These concretions lack a Gd anomaly while slightly positive Ce and
25
26 Eu anomalies are present (Table 5). The average Y/Ho of the Fe-oxy-hydroxide concretion is
27
28 23.44. Within the muddy sediments the shale-normalized REE pattern typically show weak
29
30 LREE enrichment compared to HREE (average $Pr_{SN}/Yb_{SN} = 1.1-1.2$). In particular, mud
31
32 samples have high HREE depletion compared to LREE (Pr_{SN}/Yb_{SN} up to 1.7). The average
33
34 Y/Ho ratio for the mud samples is of 25.01 (Table 6).
35
36
37
38
39
40
41
42
43
44
45
46
47

48 **4.5. Gas and Water analyses**

49
50

51 Gas samples from fast venting sites (MB14_BC05 and MB14_BC09; Tables 1, 7; Fig.
52
53 1) revealed a chemical composition dominated by CO_2 (up to 98.73% by vol.) and subordi-
54
55 nately by N_2 (up to 1.26 % by vol.) and methane (< 0.06% by vol.). The carbon and oxygen
56
57
58
59
60
61
62
63
64
65

1 isotopic ratios of CO₂ were -1.8 and -1.1 (V-PDB ‰) and -2.4 and -4.4 (V-PDB ‰), respec-
2 tively (Table 7).
3
4

5 The chemical composition (in mg L⁻¹) of the water samples collected from the rosettes
6 is reported in Table 8. The Cl⁻/Na⁺ and Cl⁻/Mg²⁺ ratios were all in a narrow range (ca. 1.8 and
7 15.5, respectively) and similar to that of the present-day seawater (Taylor and McLennan,
8 1985), whereas the Cl⁻/SO₄²⁻ and Cl⁻/K⁺ ratios were relatively more variable (mean values
9 5.89 and 46.8, respectively) and lower than that of seawater (ca. 7.2 and 48.6, respectively;
10 CRC, 2005). The concentrations of Br⁻ and F⁻ (up to 79 and 2.52 mg L⁻¹, respectively) and the
11 alkalinity (up to 243 mg L⁻¹) were slightly higher than those in the mean ocean water. Free-
12 CO₂ contents were comprised between 11.2 and 14 mmol L⁻¹.
13
14
15
16
17
18
19
20
21
22
23
24
25
26
27
28

29 **5. DISCUSSION**

30 **5.1. Characterization of authigenic minerals**

31
32
33
34
35
36 The shallow sub-bottom sediments at Paola Ridge are characterized by abundant con-
37 cretions, mainly consisting of calcite/aragonite and siderite (Table 1). Aragonite represents a
38 typical precipitate at methane seeps where microbial activity induces the increase of alkalini-
39 ty in pore solutions by AOM and the consequent precipitation of authigenic carbonates (e.g.,
40 Taviani, 2001; Peckmann and Thiel, 2004; Campbell et al., 2008; Taviani et al., 2015). At
41 methane seeps, aragonite precipitation is thought to be favored by the presence of sulfate
42 ions, which on the other hand inhibit dolomite precipitation (e.g., Magalhães et al., 2012;
43 Zhang et al., 2012). Aragonite concretions can be related to a genetic environment close to
44 the seafloor characterized by high alkalinity and sulfate concentration (e.g., Peckmann et al.,
45 2009; Hu et al., 2014). The precipitation of authigenic aragonite and calcite at Paola Ridge
46
47
48
49
50
51
52
53
54
55
56
57
58
59
60
61
62
63
64
65

1 only occurs within the sediments of D1 and D2 diapirs, near the seafloor within the SMTZ
2 (Rovere et al., 2014, 2015) during periods of moderate to intense seepage when SMTZ mi-
3 grates upward. In the calcite/aragonite samples, dolomite is only found as thin crust lining the
4 calcite/aragonite concretions and it is likely precipitated at a different stage of the seepage.
5
6
7
8
9
10 Precipitation of dolomite is indeed favored by low concentrations of sulfate (Magalhães et al.,
11 2012) and therefore is unlikely to form together with aragonite or at present day conditions
12 with up to 3918 mg L⁻¹ of SO₄²⁻ in the bottom seawater (Table 8). Nevertheless, recent stud-
13 ies demonstrated how high sulfide concentration, rather than low sulfate, favors dolomite
14 precipitation at sites of methane seepage (Zhang et al., 2012; Taviani et al., 2015). At times
15 of intense seepage the sulfate-methane transition zone (SMTZ) is pulled further upward
16 through the subseafloor sediment and the sulfates in the shallow sediments are more efficient-
17 ly consumed releasing Mg-ions. Consequently, under such conditions the Mg/Ca ratio in-
18 creases and dolomite precipitates (e.g., Magalhães et al., 2012). In this scenario the precipita-
19 tion of dolomite likely records an additional surge in seepage activity following the first
20 seepage increase responsible for aragonite/calcite concretion precipitation.
21
22
23
24
25
26
27
28
29
30
31
32
33
34
35
36

37 Pyrite is another common authigenic mineral found at methane seeps (e.g., Peckmann
38 and Thiel, 2004; Cavalazzi et al., 2014) where the bacterial-mediated sulfate reduction fosters
39 the precipitation of pyrite rather than siderite (e.g., Curtis et al., 1972). Interestingly, in the
40 study area, pyrite and siderite are characteristic of the core sediments from the RMV and
41 RIMV structures, where carbonate/aragonite concretions are lacking (Fig. 2). However, py-
42 rite and siderite never co-occur in the same concretion (Table 1; Figs. 2-6). Mozley and
43 Wersin (1992) demonstrated that siderite precipitation is favored by suboxic conditions cou-
44 pled with low organic matter content and low sedimentation rate, and strongly reducing con-
45 ditions. Generally, siderite formation is favored by low sulfide activity under anoxic condi-
46 tions (Taylor and Curtis, 1995; Rovere et al., 2015) and therefore occurs outside the sulfate
47
48
49
50
51
52
53
54
55
56
57
58
59
60
61
62
63
64
65

1 reduction zone, where organic matter fermentation (i.e. methanogenic zone) occurs (Matsu-
2 moto, 1989; Mozley and Carothers, 1992; Hicks et al., 1996; Hein et al., 2006; Wittkop et al.,
3
4 2014). The methanogenic zone provides conditions suitable for preferential precipitation of
5 siderite (e.g., Berner, 1981; Mozley and Wersin, 1992) with respect to that of pyrite (e.g.,
6
7 Rovere et al., 2015). Therefore, the co-occurrence of pyrite and siderite in single sampling
8
9 sites has to be explained with the dynamics of the environment itself and must be related to
10
11 fluctuation in the intensity of fluids seepage and gas venting. On RMV and RIMV structures,
12
13 during periods of sustained gas venting, the abundance of sulfate within the sea water in-
14
15 creases (Table 8) and sulfate reduction favors pyrite precipitation and would inhibit siderite
16
17 precipitation. This hypothesis is supported by the concentrations of SO_4^{2-} at the bottom sea-
18
19 water (Table 8), which were >20% higher than that of the Mediterranean Sea. During periods
20
21 of lower gas discharges the SMTZ deepens and decreased sulfide concentration is associated
22
23 with the increase of dissolved Fe^{2+} in the shallow sub-bottom sediments, thus facilitating the
24
25 precipitation of siderite (e.g., Curtis et al., 1972).
26
27
28
29
30
31
32
33
34
35
36

37 **5.2. Isotopic composition of carbonates and origin of mineralizing fluids**

38
39

40 The calcite/aragonite concretions are characterized by negative $\delta^{13}\text{C}$ values (-48.8‰
41 to -26.3‰ V-PDB; Table 1) indicating ^{13}C -poor dissolved inorganic carbon (DIC) issued
42 from methane oxidation as the source of carbon (e.g., Whiticar, 1999; Peckmann and Thiel,
43 2004). The variable carbon isotopic composition of the samples is likely indicative of mixing
44 between thermogenic and biogenic methane-rich fluids (e.g., Mazzini et al., 2005; Peckmann
45 and Thiel, 2004), or fractionation processes as the methane-rich fluids migrate.
46
47
48
49
50
51
52
53

54 Siderite concretions, on the other hand, show highly positive $\delta^{13}\text{C}$ values (between
55 3.2‰ and 10.6‰ V-PDB), which suggests precipitation from fluids with ^{13}C -rich DIC. These
56
57
58
59
60
61
62
63
64
65

1 positive $\delta^{13}\text{C}$ values can be diagnostic of precipitation in the methanogenic zone (e.g., Curtis
2 and Coleman, 1986; Mozley and Wersin, 1992; Whiticar, 1999). Whilst the $\delta^{18}\text{O}$ values of
3 calcite/aragonite concretions ranged between 1.4‰ and 5.5‰ V-PDB, the average $\delta^{18}\text{O}$ for
4 siderite is greater than 9‰ V-PDB. At the average value of the present-day bottom water
5 temperature (13.8 °C) and $\delta^{18}\text{O}$ value of water (1.5‰) in the Mediterranean Sea, the theoreti-
6 cal $\delta^{18}\text{O}$ values of calcite (Kim and O'Neil, 1997), aragonite (Kim et al., 2007), dolomite
7 (Vasconcelos et al., 2005) and siderite (Fernandez et al., 2016) precipitated in isotopic equi-
8 librium with seawater are expected to be of 1.5‰, 2.2‰, 4.5‰ and 5.6‰ (V-PDB), respec-
9 tively. The $\delta^{18}\text{O}$ values obtained from the Paola Ridge carbonates approach the theoretical
10 values except for those of siderite, which are mostly enriched in ^{18}O by 3 to 4‰.

11
12
13
14
15
16
17
18
19
20
21
22
23
24
25 Whilst general ^{13}C enrichment can be explained with the incorporation of heavy C de-
26 rived from methanogenesis the enrichment of ^{18}O is more cumbersome. The ^{18}O enrichment
27 in carbonates has previously been explained by different processes occurring in the sedimen-
28 tary environment, as follows: 1) dissociation of gas hydrates that releases ^{18}O -rich water in
29 the sediments (e.g., Bohrmann et al., 1998; Aloisi et al., 2000; Maekawa, 2004; Hein et al.,
30 2006); 2) interaction with hydrothermal fluids that may yield values as high as 6.5‰ (Clay-
31 ton and Epstein, 1961); 3) dehydration of clay minerals at great burial depths (Dählmann and
32 de Lange, 2003); 4) crustal/igneous CO_2 circulation (Muehlenbachs and Hodges, 1978;
33 Clayton and Epstein, 1961; Cocker et al., 1982); 5) precipitation of carbonates during glacial
34 times when lower temperatures and isotopically heavier seawater caused a 3 to 4‰ $\delta^{18}\text{O}$ -shift
35 of carbonates in the Mediterranean Sea (e.g., Vergnaud-Grazzini, 1971). Other sources of
36 heavy oxygen can be due to the circulation of deep crustal water (e.g., Lécuyer and
37 Allemand, 1999). Lécuyer and Allemand (1999) discussed how the significant enrichment in
38 ^{18}O of ophiolitic complexes (up to 8‰; Lécuyer and Fourcade, 1991) would explain the shift
39 toward higher $\delta^{18}\text{O}$ values of the circulating water. These authors proved that at depth be-
40
41
42
43
44
45
46
47
48
49
50
51
52
53
54
55
56
57
58
59
60
61
62
63
64
65

1
2
3
4
5
6
7
8
9
10
11
12
13
14
15
16
17
18
19
20
21
22
23
24
25
26
27
28
29
30
31
32
33
34
35
36
37
38
39
40
41
42
43
44
45
46
47
48
49
50
51
52
53
54
55
56
57
58
59
60
61
62
63
64
65

tween 1.5 and 3.5 km the increase of temperature induces a large oxygen fractionation between the igneous rocks and seawater resulting in lower $\delta^{18}\text{O}$ values within the rocks at the expense of the reacting water.

The presence of active venting of CO_2 along RMV and R1MV (Tables 1, 7) suggests that the likely source of heavy oxygen isotopes in siderite concretions can be related to deep fluids circulation (e.g., Clayton and Epstein, 1961; Lécuyer and Allemand, 1999; Lietard and Pierre, 2009). The presence of CO_2 -rich gas discharges, characterized by $\delta^{13}\text{C}\text{-CO}_2$ values slightly lower than -1‰ V-PDB (Table 7), certainly suggests the presence of a deep-seated (hydrothermal) source feeding these gas vents. Such values are indeed similar to those found in the fumarolic gas discharges from the Island of Volcano (e.g., Paonita et al., 2002) and Solfatara, Somma-Vesuvius and related submarine emissions (e.g., Chiodini et al., 2001; Caliro et al., 2007; Vaselli et al., 2011; Passaro et al., 2016) and many gas vents distributed along the peri-Tyrrhenian strip (e.g., Minissale et al., 1997) of the Italian peninsula. The origin of the peri-Tyrrhenian vents is mainly related to thermometamorphic processes of marine limestone, although small contributions from a magmatic source cannot be excluded. In addition, the concentrations of free- CO_2 within the Paola Ridge bottom sea water showed relatively high values, which corroborate the contribution of deep-seated CO_2 to the gas discharges. At Paola Ridge CO_2 -rich-gas venting was only recorded along the RMV and R1MV structures suggesting a possible interaction between CO_2 venting and siderite precipitation and therefore a likely ^{18}O enrichment of the iron carbonates related to crustal/igneous CO_2 circulation (Muehlenbachs and Hodges, 1978; Clayton and Epstein, 1961; Cocker et al., 1982). Although CO_2 -rich sediments are usually considered unsuitable for carbonate precipitation, siderite precipitation has previously been reported at the oxic-suboxic transition in places where venting CO_2 reacts with reduced iron within the sediments (Bahrig, 1988; Mozley and Wersin, 1992).

1
2
3
4
5
6
7
8
9
10
11
12
13
14
15
16
17
18
19
20
21
22
23
24
25
26
27
28
29
30
31
32
33
34
35
36
37
38
39
40
41
42
43
44
45
46
47
48
49
50
51
52
53
54
55
56
57
58
59
60
61
62
63
64
65

Rovere et al. (2014) performed AMS radiocarbon age dating on chemosymbiotic bivalves collected from the shallow sediments of the Paola Ridge (alongside diapirs D1 and D2) revealing calibrated age ranging between 440 BP and 13710 BP suggesting a prolonged seepage activity. Notwithstanding, investigations on present day venting gas and bottom sea water highlighted the absence of substantial concentrations of methane (Tables 7, 8). Normally, at sites of vigorous methane seepage the presence of methane can be detected within samples of water throughout the water column up to very shallow depth (see Sommer et al., 2015) and gas bubbles at the surface might still contain up to 25% of the original methane (Sommer et al., 2015; von Deimling et al., 2015). Nevertheless, as far as the sampled waters are concerned, their chemical composition is approaching that of the oceanic water reported by Taylor and McLennan (1985), though slightly more alkaline (Table 8), as typical of relatively closed basin such as the Mediterranean Sea. The general lack of methane in both venting gases and bottom sea water at Paola Ridge suggests that the methane seepage, active for the last 10k year (40k years according to Rovere et al., 2015), is currently minimal.

5.3. Redox conditions during sedimentation

40
41
42
43
44
45
46
47
48
49
50
51
52
53
54
55
56
57
58
59
60
61
62
63
64
65

The distribution of the studied samples is likely reflecting a biogeochemical zonation of the sediments from oxic conditions to AOM/sulfate reduction to methanogenesis (Rovere et al., 2015), being influenced by fluctuation of seepage activity. The REE pattern of marine carbonates can be used as a geochemical proxy for the reconstruction of fluid composition and physical-chemical variations (e.g., Franchi et al., 2015; 2016 and references therein). Several studies showed that REE are not affected by fractionation processes during precipitation of aragonite and calcite (see discussion in Rongemaille et al., 2011) whereas REE distribution tends to vary significantly in sediments according to the redox variations within the pore water (e.g., Haley et al., 2004). Nevertheless, the use of carbonates as a proxy for the

1 REE content of ancient seawater is complicated by possible modification due to the presence
2 of: i) REE-bearing terrigenous components (Goldstein and Jacobsen, 1988; Elderfield et al.,
3 1990); ii) Fe-Mn-oxy-hydroxides (Bau et al., 1996; Bayon et al., 2004) and iii) phosphates,
4 which might have a non-uniform REE incorporation (German and Elderfield, 1990; Byrne et
5 al., 1996). To avoid the terrigenous contamination, Rongemaille et al. (2011) proposed the
6 usage of weak acetic acid solution (5% v/v) for quantitative leaching of carbonate samples
7 with the exception of siderite. Considering that a weak acid leaching is not appropriate to
8 achieve complete dissolution of siderite, a total dissolution method has been adopted here and
9 possible contaminations were verified by using a correlative method (Fig. 9).

10
11
12
13
14
15
16
17
18
19
20
21
22
23 Normalized calcite/aragonite REE patterns (Fig. 7A) displayed a non-marine seawater
24 trend in the study samples (e.g., Zhang and Nozaki, 1996). Terrigenous compounds, in par-
25 ticular clay minerals, within carbonate rocks are able to mask the seawater signature (e.g.,
26 Murray et al., 1991; Oliver and Boyet, 2006). Al₂O₃, SiO₂, Zr and Rb distributions are con-
27 sidered proxies for concentrations of terrigenous minerals since they closely correlate with
28 the clay content. Despite the high Al₂O₃ and SiO₂ contents (weight % on the bulk sample;
29 Table 2), there is no clear correlation ($R^2=0.52$ and 0.54 , respectively) with LREE and Σ REE
30 (Fig. 9A-D). On the other hand, Zr and Rb are weakly correlated with Σ REE (Fig. 9F, G),
31 suggesting a possible minor contribution from acid-leached terrigenous minerals to the over-
32 all REE budget (Fig. 9A-G). Other potential contaminants, such as Fe- and P-compounds
33 (German and Elderfield, 1990; Bau et al., 1996; Reynard et al., 1999; Bayon et al., 2004; Bau
34 and Koschinsky, 2009) do not show significant correlations with Σ REE and LREE (Fig. 9H-
35 I). A flat REE patten and lack of a Ce anomaly indicate that the calcite/aragonite concretions
36 incorporated high amounts of organic matter and precipitated within relatively highly alkaline
37 pore water (e.g., Pourret et al., 2008). Hypothetical mixing patterns between the limestone
38 and Fe-oxy-hydroxide components do not produce any sensible variation in the REE frac-
39
40
41
42
43
44
45
46
47
48
49
50
51
52
53
54
55
56
57
58
59
60
61
62
63
64
65

1 tionation, even though the REE content considerably increases (Fig. 10A). Both limestone
2 and Fe-oxy-hydroxide REE patterns are relatively flat (average $Pr_{SN}/Yb_{SN}=1.10$ and 1.01,
3 respectively) with a slight MREE enrichment ($Gd_{SN}/Yb_{SN}=1.28$ and 1.45, respectively),
4 which is typical of precipitates formed in oxic to sub-oxic pore water (Haley et al., 2004).
5 Under such conditions the REE pattern lacks Ce and Gd anomalies and the precipitates are
6 expected to inherit these characteristics from the reacting water.
7
8
9

10
11
12
13
14
15 The REE patterns of the siderite concretions (Fig. 8) show a general depletion of
16 LREE and a quasi-marine trend (cf. Zhang and Nozaki, 1996) with strong HREE enrichment
17 with respect to LREE. Within siderite samples Al_2O_3 , SiO_2 , Rb and Zr do not correlate with
18 LREE and Σ REE (Fig. 9A-E) ruling out any terrigenous contamination. Similarly, contami-
19 nation by Fe-Mn-oxy-hydroxides and phosphates can be considered negligible or absent as
20 no correlation between Fe and P and LREE and Σ REE is recorded (Fig. 9H, I). Nevertheless,
21 the hypothetical siderite and Fe-oxy-hydroxide mixing (Fig. 10B) shows that i) the increase
22 of Fe-oxy-hydroxides incorporation in the siderite concretions induces a general increase of
23 LREE concentration and a flattening of the REE pattern similar to that detected in the aver-
24 age limestone concretions and ii) siderite and Fe-oxy-hydroxide have an opposite rate of Y
25 complexation and similar HREE concentration.
26
27
28
29
30
31
32
33
34
35
36
37
38
39
40
41
42

43 The lack of LREE fractionation in the Fe-oxy-hydroxides from Paola Ridge (Fig. 7)
44 may be due to a rapid deposition (e.g., Bau and Dulski, 1996) under oxic conditions. In con-
45 trast, the strong LREE fractionation found in the siderite concretions points toward a slow
46 formation close to the exchange equilibrium of adsorbed/dissolved REE and Y (Bau and
47 Dulski, 1996) under reducing conditions (see Fig. 1 in Mozley and Wersin, 1992). The pro-
48 longed anoxic conditions, high pore water alkalinity and high Fe concentration are also sug-
49 gested by the enrichment of MREE (Haley et al., 2004) and the lack of a Ce anomaly (see
50 discussion below). The siderite precipitation rate is eight orders of magnitude slower than
51
52
53
54
55
56
57
58
59
60
61
62
63
64
65

1 that of calcite (Jimenez-Lopez and Romanek, 2004) and therefore, the formation of siderite
2 concretions is likely to be stable under supersaturated conditions fostering LREE fractiona-
3 tion.
4
5
6
7

8 The value of the Ce anomaly is thought to be indicative of redox state (Haley et al.,
9 2004 and citations therein), being negative (ca. 0.2-0.4) under oxygenated conditions and
10 positive under anoxic conditions (e.g., Oliver and Boyet, 2006; Hu et al., 2014; Tostevin et
11 al., 2016). Nevertheless, the presence/absence of a negative Ce anomaly in authigenic me-
12 thane-imprinted carbonates is due to mineral formation in high pore water alkalinity where
13 organic matter occurs (Pourret et al., 2008; Kim et al., 2012) and/or to the intermittent oxy-
14 genation of sediments (Birgel et al., 2011; Hu et al., 2014). In the case under investigation the
15 latter scenario, with alternating anoxic, suboxic conditions, discontinuous fluids discharge
16 and downward flow of sea water during periods of reduced seepage can produce carbonates
17 with a particular geochemical signature and disguise the original Ce anomaly (Solomon et al.,
18 2008; Kim et al., 2012; Hu et al., 2014) resulting in a Ce/Ce* ratio close to 1. The lack of a
19 Ce anomaly, typical of both limestone and siderite at the Paola Ridge (Tables 2-3) can thus
20 be explained by discontinuity of methane seepage and sustained conditions of high alkalinity
21 and high organic matter content.
22
23
24
25
26
27
28
29
30
31
32
33
34
35
36
37
38
39
40
41
42

43 As discussed above, siderite concretions at Paola Ridge show heavy carbon composi-
44 tion, which is typical of the fermentation zone occurring at deeper sub-bottom settings (e.g.,
45 Irwin et al., 1977; Matsumoto, 1989; Wittkop et al., 2014). In such a setting the high alkalini-
46 ty and the preferential uptake of dissolved Ce(IV) by organic compounds induces a Ce en-
47 richment in the authigenic fraction (Pourret et al., 2008; Kim et al., 2012; Hu et al., 2014).
48 Therefore authigenic siderite formed within the methanogenesis zone, where metabolic activ-
49 ity of microbial consortia within organic matter-rich sediments increases pore water alkalinity
50
51
52
53
54
55
56
57
58
59
60
61
62
63
64
65

1 triggering the precipitation of authigenic carbonates (e.g., Chafetz and Buczynski, 1992;
2 Monty, 1995), may also lack a consistent Ce anomaly.
3
4

5 The variation in redox condition during the formation of authigenic carbonates can be
6 outlined by using specific trace elements such as Mo and U (e.g., Hu et al., 2014). In well-
7 oxygenated water Mo behaves conservatively, whereas it normally enriches within organic
8 matter and iron sulfides under anoxic conditions (Helz et al., 1996; Neubert et al., 2008;
9 Algeo and Tribovillard, 2009). In anoxic conditions Mo is completely removed from sea-
10 water and accumulates in surface sediments (Neubert et al., 2008). Under oxic conditions U
11 is present in its oxidized form U(VI) showing a conservative behavior (e.g., Hu et al., 2014),
12 whereas in suboxic conditions (within the iron reduction zone) U(VI) is reduced to the insol-
13 ule U(IV), the uptake of which is facilitated by the presence of organic matter. The overall
14 Mo/U ratio decreases in the iron reduction zone. Molybdenum content in all but two car-
15 bonate concretions (Cal-C and Cal-N) is consistently greater than the crustal average (1-2
16 ppm; Taylor and McLennan, 1985) and much higher than that expected for pure carbonate
17 rocks (0.02 ppm; Neubert et al., 2008). The high Mo contents in calcite/aragonite (average
18 18.3 ppm), siderite (average 36.4 ppm) and sulfide (average 111.2 ppm) concretions point
19 toward suboxic to anoxic conditions during carbonate precipitation. Whether suboxic
20 authigenic carbonates retain moderate Mo content (up to 25 ppm) and low $(\text{Mo}/\text{U})_{\text{EF}}^1$ values,
21 sediments precipitated in euxinic conditions yield a much greater Mo content (>60 ppm; Hu
22 et al., 2014) and $(\text{Mo}/\text{U})_{\text{EF}}$ values (Algeo and Tribovillard, 2009). Anomalously high Mo
23 concentrations are believed to reflect the formation of iron sulfides after the production of
24 hydrogen sulfide during AOM (Sato et al., 2012; Hu et al., 2014). Therefore, high $(\text{Mo}/\text{U})_{\text{EF}}$
25 ratios and Mo enrichment are considered to evidence the precipitation in a sulfidic conditions
26
27
28
29
30
31
32
33
34
35
36
37
38
39
40
41
42
43
44
45
46
47
48
49
50
51
52
53
54
55
56

57
58 ¹ $X_{\text{EF}} = [(X/\text{Al})_{\text{sample}} / (X/\text{Al})_{\text{PAAS}}]$, where X and Al represent the concentrations of the elements X and the
59 weight concentrations of Al_2O_3 (Algeo and Tribovillard, 2009)
60
61
62
63
64
65

1 (Hu et al., 2014). Sulfidic conditions vary with the seepage activity and AOM-derived hydro-
2 gen sulfide and may spread from the shallow sediments to the water column producing
3 anomalously high Mo enrichment (Sato et al., 2012; Hu et al., 2014). The anomalously high
4 concentration of Mo in Paola Ridge authigenic carbonates is produced at times of intense
5 seepage. During periods of lower discharge downward migration of seawater oxidizes AOM-
6 generated hydrogen sulfide. This implies that hydrogen sulfide is maintained at a low level
7 for Mo enrichment and Fe-sulfides formation. Whilst calcite/aragonite shows average
8 $(\text{Mo/U})_{\text{EF}}$ of 2.88, reflecting precipitation from sulfidic pore water, dolomite crusts show
9 $(\text{Mo/U})_{\text{EF}}$ values as low as 0.31 reflecting a much lower sulfide concentration (Algeo and
10 Tribovillard, 2009; Hu et al., 2014) likely related to a lower methane flux. Siderite, on the
11 other hand, yields higher $(\text{Mo/U})_{\text{EF}}$ values (average 32.2), which are evidence of precipitation
12 under strong anoxic conditions.

13
14
15
16
17
18
19
20
21
22
23
24
25
26
27
28
29
30 Varying $(\text{Mo/U})_{\text{EF}}$, Ce anomalies and carbonate phases are better explained by tempo-
31 rary oxic conditions and variations in sulfide concentration induced by seepage flux changes
32 (Feng et al. 2009; Birgel et al., 2011; Hu et al., 2014). These changes have probably been
33 triggered by allogenic rapid changes in palaeoenvironmental and palaeoceanographic condi-
34 tions (Rovere, unpublished data). It is important to note how calcite/aragonite and siderite
35 concretions never co-occur, revealing a likely difference in the seepage conditions along
36 R1MV and RMV, where ^{13}C -rich siderite occurs, and along the mud diapirs, where siderite is
37 lacking but ^{13}C -poor AOM-related calcite/aragonite concretions are abundant.

38 39 40 41 42 43 44 45 46 47 48 49 50 51 52 **6. CONCLUDING REMARKS**

53
54
55 Authigenic mineral concretions were collected in shallow sub-bottom sediments at the
56 Paola Ridge (Southern Tyrrhenian Sea) along two alleged mud volcanoes (RMV and R1MV)
57 and two diapirs (D1 and D2). A complete array of geochemical analyses has been performed

1 to unravel the effects of discontinuous methane seepage on the genesis and early diagenesis
2 of shallow sub-bottom sediments. Authigenic minerals, including calcite/aragonite, siderite,
3 sulfide and Fe-oxy-hydroxide, venting gases and bottom seawater have been analyzed.
4
5
6

7
8 Calcite/aragonite concretions yielded negative $\delta^{13}\text{C}$ values (as low as -48.8‰) and
9 positive $\delta^{18}\text{O}$ (up to 5.5‰ V-PDB) values. Negative $\delta^{13}\text{C}$ values together with the presence
10 of chemosymbiotic bivalves are characteristic of a precipitation of calcite and aragonite with-
11 in the AOM zone. Evidences of AOM are restricted to the D1 and D2 diapirs. The presence
12 of dolomite crusts lining calcite/aragonite concretions is *per se* an evidence of variation in the
13 sulfate concentration induced by variation in the seepage activity and therefore vertical fluc-
14 tuation of the SMTZ. Along D1 and D2 calcite/aragonite precipitate at time of moderate to
15 high methane flux within the SMTZ close to the seafloor, under the influence of bottom sea-
16 water. Dolomite crusts precipitated at time of i) low methane flux (low sulfide concentra-
17 tions) or ii) extremely vigorous methane seepage (high sulfite concentrations). The low
18 $(\text{Mo}/\text{U})_{\text{EF}}$ ratio in the studied samples points toward the latter. This scenario of discontinu-
19 ous seepage is corroborated by the REE distribution and trace elements concentration, and
20 particularly by the lack of a Ce anomaly and the $(\text{Mo}/\text{U})_{\text{EF}}$ within the authigenic minerals.
21 Whilst Mo enrichment points toward strongly anoxic and sulfidic conditions, the lack of a Ce
22 anomaly suggests episodes of low seepage activity characterized by downward migration of
23 bottom seawater.
24
25
26
27
28
29
30
31
32
33
34
35
36
37
38
39
40
41
42
43
44
45
46

47
48 On the other hand the structures previously described as mud volcanoes (RMV and
49 R1MV), where CO_2 -rich gas venting is active at the seafloor, show ca. 6 m of highly de-
50 formed mud lacking any evidence of AOM. RMV and R1MV sediments are rich in sulfide
51 concretions and siderite. Siderite concretions are characterized by strong enrichments in both
52 heavy carbon and heavy oxygen isotope with average $\delta^{13}\text{C}$ and $\delta^{18}\text{O}$ values of 10.6‰ and
53
54
55
56
57
58
59
60
61
62
63
64
65

1
2
3
4
5
6
7
8
9
10
11
12
13
14
15
16
17
18
19
20
21
22
23
24
25
26
27
28
29
30
31
32
33
34
35
36
37
38
39
40
41
42
43
44
45
46
47
48
49
50
51
52
53
54
55
56
57
58
59
60
61
62
63
64
65

9.9‰ (V-PDB), respectively. Along RMV and R1MV during periods of high flux the abundance of sulfate and Fe active ions fostered the precipitation of pyrite at the expenses of siderite. During periods of lower gas discharges the SMTZ deepens and the decreased sulfide concentration, associated with the increase of dissolved Fe²⁺, facilitates the precipitation of siderite. Siderite precipitation occurred under prolonged anoxic conditions as shown by LREE fractionation and high (Mo/U)_{EF}. Most likely the precipitation of siderite took place within the methanogenic zone, as suggested by ¹³C enrichment, and was affected by intense crustal CO₂ venting that induced sensible ¹⁸O enrichment. The presence of intense ongoing CO₂-rich gas discharges, characterized by δ¹³C-CO₂ values slightly <-1 ‰ V-PDB, along RMV and R1MV structures and the Y/Ho chondritic ratios of the carbonates suggest the presence of a deep-seated source feeding these gas vents. The lack of consistent methane concentrations within the bottom sea water, coupled with lack of AOM precipitates, suggests that RMV and R1MV structures are not related to seepage of biogenic or thermogenic methane and cannot unambiguously be considered mud volcanoes.

The combination of trace elements (i.e. Mo and U) and REE shed light onto a complex scenario where episodic variations of seepage activity, redox condition and SMTZ fluctuation induced precipitation of diverse authigenic phases. Similar considerations apply to other modern and fossil cold seep sites and provide alternative scenario for the genesis and early diagenesis of authigenic precipitates.

ACKNOWLEDGEMENTS

1
2
3 Thanks are due to L. Giannini (Department of Earth Sciences, University of Florence) and
4
5 E.M. Selmo (Department of Physics and Earth Sciences, University of Parma) for the gas
6
7 sampling and the isotopic analyses of the carbonates, respectively. FF thanks T.O. Bineli
8
9 Betsi (BIUST) for the precious advices concerning sulfides petrography. Thanks are due to
10
11 Graeme Bremner (BIUST) for proofreading the manuscript.
12
13
14
15

16 This research was supported by the flagship project Ritmare (www.ritmare.it) funded by the
17
18 Italian Ministry of Research and Education (MIUR).
19
20
21
22
23
24
25
26
27
28
29
30
31
32
33
34
35
36
37
38
39
40
41
42
43
44
45
46
47
48
49
50
51
52
53
54
55
56
57
58
59
60
61
62
63
64
65

REFERENCES

- 1
2
3 Al-Aasm, I.S., Taylor, B.E., South, B., 1990. Stable isotope analysis of multiple carbonate
4 samples using selective acid extraction. *Chem. Geol.* 80, 119-125.
5
6
7
8
9 Algeo, T., Tribovillard, N., 2009. Environmental analysis of paleoceanographic systems
10 based on molybdenum–uranium covariation. *Chem. Geol.*, 268, 211-225.
11
12
13
14 Allwood, A.C., Kamber, B.S., Walter, M.R., Burch, I.W., Kanik, I., 2010. Trace elements
15 record depositional history of an Early Archean stromatolitic carbonate platform.
16
17
18
19
20
21
22
23 Aloisi, G., Pierre, C., Rouchy, J.-M., Foucher, J.-P., Woodside, J., 2000. Methane-related
24 authigenic carbonates of eastern Mediterranean Sea mud volcanoes and their possible
25
26
27
28
29
30
31
32
33
34
35
36
37
38
39
40
41
42
43
44
45
46
47
48
49
50
51
52
53
54
55
56
57
58
59
60
61
62
63
64
65
- Al-Aasm, I.S., Taylor, B.E., South, B., 1990. Stable isotope analysis of multiple carbonate samples using selective acid extraction. *Chem. Geol.* 80, 119-125.
- Algeo, T., Tribovillard, N., 2009. Environmental analysis of paleoceanographic systems based on molybdenum–uranium covariation. *Chem. Geol.*, 268, 211-225.
- Allwood, A.C., Kamber, B.S., Walter, M.R., Burch, I.W., Kanik, I., 2010. Trace elements record depositional history of an Early Archean stromatolitic carbonate platform. *Chem. Geol.* 270, 148-163.
- Aloisi, G., Pierre, C., Rouchy, J.-M., Foucher, J.-P., Woodside, J., 2000. Methane-related authigenic carbonates of eastern Mediterranean Sea mud volcanoes and their possible relation to gas hydrate destabilisation. *Earth Planet. Sci. Lett.* 184, 321-338.
- Angeletti, L., Canese, S., Franchi, F., Montagna, P., Reitner, J., Walliser, E.O., Taviani, M., 2015. The chimney forest of the deep Montenegrin margin, south-eastern Adriatic Sea. *Mar. Petrol. Geol.* 66, 542-554.
- Bahrig, B., 1988. Palaeo-environment information from deep water siderite (Lake of Laach, West Germany). *In: Fleet, A.J., et al. [Eds.] Lacustrine petroleum source rocks. Geological Society of London Special Publication 40, 153-158.*
- Bau, M., 1996. Controls on the fractionation of isovalent trace elements in magmatic and aqueous systems: evidence from Y/Ho, Zr/Hf, and lanthanide tetrad effect. *Contrib. Mineral. Petrol.* 123, 323-333.

- 1
2
3
4
5
6
7
8
9
10
11
12
13
14
15
16
17
18
19
20
21
22
23
24
25
26
27
28
29
30
31
32
33
34
35
36
37
38
39
40
41
42
43
44
45
46
47
48
49
50
51
52
53
54
55
56
57
58
59
60
61
62
63
64
65
- Bau, M., Dulski, P., 1996. Distribution of yttrium and rare-earth elements in the Penge and Kuruman iron-formations, Transvaal Supergroup, South Africa. *Precambrian Res.* 79, 37-55.
- Bau, M., Dulski, P., 1999. Comparing yttrium and rare earths in hydrothermal fluids from the Mid-Atlantic Ridge: implications for Y and REE behaviour during near-vent mixing and for the Y/Ho ratio of Proterozoic seawater. *Chem. Geol.* 155, 77-90.
- Bau, M., Koschinsky, A., 2009. Oxidative scavenging of cerium on hydrous Fe oxide: evidence from the distribution of rare earth elements and yttrium between Fe oxides and Mn oxides in hydrogenetic ferromanganese crusts. *Geochem. J.* 43, 37-47.
- Bau, M., Koschinsky, A., Dulski, P., Hein, J.R., 1996. Comparison of the partitioning behaviours of yttrium, rare earth elements, and titanium between hydrogenetic marine ferromanganese crusts and seawater. *Geochim. Cosmochim. Acta* 60, 1709-1725.
- Bau, M., Möller, P., Dulski, P., 1997. Yttrium and lanthanides in eastern Mediterranean seawater and their fractionation during redox-cycling. *Mar. Chem.* 56, 123-131.
- Bayon, G., German, C.R., Burton, K.W., Nesbitt, R.W., Rogers, N., 2004. Sedimentary Fe–Mn oxy-hydroxides as paleoceanographic archives and the role of aeolian flux in regulating oceanic dissolved REE. *Earth Planet. Sci. Lett.* 224, 477-492.
- Berner, R.A., 1981. A new geochemical classification of sedimentary environments. *J. Sediment. Petrol.* 51, 359-365.
- Birgel, D., Feng, D., Roberts, H.H., Peckmann, J., 2011. Changing redox conditions at cold seeps as revealed by authigenic carbonates from Alaminos Canyon, northern Gulf of Mexico. *Chem. Geol.* 285, 82-96.

- 1
2
3
4
5
6
7
8
9
10
11
12
13
14
15
16
17
18
19
20
21
22
23
24
25
26
27
28
29
30
31
32
33
34
35
36
37
38
39
40
41
42
43
44
45
46
47
48
49
50
51
52
53
54
55
56
57
58
59
60
61
62
63
64
65
- Blumenberg, M., Walliser, E.O., Taviani, M., Seifert, R., Reitner, J., 2015. Authigenic carbonate formation and its impact on the biomarker inventory at hydrocarbon seeps – A case study from the Holocene Black Sea and the Plio-Pleistocene Northern Apennines (Italy). *Mar. Petrol. Geol.* 66, 532-541.
- Boetius, A., Suess, E., 2004. Hydrate Ridge: A natural laboratory for the study of microbial life fueled by methane from near-surface gas hydrates. *Chem. Geol.* 205, 291-310.
doi:10.1016/j.chemgeo.2003.12.034
- Boetius, A., Ravenschlag, K., Schubert, C.J., Rickert, D., Widdel, F., Gieseke, A., Amann, R., Jørgensen, B.B., Witte, U., Pfannkuche, O., 2000. A marine microbial consortium apparently mediating anaerobic oxidation of methane. *Nature* 407, 623-626.
- Bohrmann, G., Greinert, J., Suess, E., Torres, M.E., 1998. Authigenic carbonates from the Cascadia subduction zone and their relation to gas hydrate stability. *Geology* 26, 647-650.
- Byrne, R.H., Liu, X., Schijf, J., 1996. The influence of phosphate coprecipitation on rare earth element distributions in natural waters. *Geochim. Cosmochim. Acta* 60, 3341-3346.
- Cabassi J., Vaselli, O., Tassi, F., Giannini, L., 2011. Studio idrogeochimico delle acque sotterranee nella porzione settentrionale del Comune di Arezzo. Internal report; Department of Earth Sciences – University of Florence (Italy), p. 42. (In Italian).
- Caliro, S., Chiodini, G., Moretti, R., Avino, R., Granieri, D., Russo, M., Fiebig, J., 2007. The origin of the fumaroles of La Solfatara (Campi Flegrei, South Italy). *Geochim. Cosmochim. Acta*, 71, 3040-3055.

- 1
2
3
4
5
6
7
8
9
10
11
12
13
14
15
16
17
18
19
20
21
22
23
24
25
26
27
28
29
30
31
32
33
34
35
36
37
38
39
40
41
42
43
44
45
46
47
48
49
50
51
52
53
54
55
56
57
58
59
60
61
62
63
64
65
- Campbell, K.A., Francis, D.A., Collins, M., Gregory, M.R., Nelson, C.S., Greinert, J., Aharon, P., 2008. Hydrocarbon seep-carbonates of a Miocene forearc (East Coast Basin), North Island, New Zealand. *Sediment. Geol.* 204, 83-105.
- Cangemi, M., Di Leonardo, R., Bellanca, A., Cundy, A., Neri, R., Angelone, M., 2010. Geochemistry and mineralogy of sediments and authigenic carbonates from the Malta Plateau, Strait of Sicily (Central Mediterranean): Relationships with mud/fluid release from a mud volcano system. *Chem. Geol.* 276, 294-308. doi:10.1016/j.chemgeo.2010.06.014
- Capozzi, R., Guido, F.L., Oppo, D., Gabbianelli, G., 2012. Methane-derived authigenic carbonates (MDAC) in northern-central Adriatic Sea: relationships between reservoir and methane seepages. *Mar. Geol.* 332-334, 174-188.
- Carothers, W.W., Adami, L.H., Rosenbauer, R.J., 1988. Experimental oxygen isotope fractionation between siderite-water and phosphoric acid liberated CO₂-siderite. *Geochim. Cosmochim. Acta* 52, 2445-2450.
- Cau, S., Franchi, F., Roveri, M., Taviani, M., 2015. The Pliocene-age Stirone River hydrocarbon chemoherm complex (Northern Apennines, Italy). *Mar. Petrol. Geol.* 66, 582-595.
- Cavalazzi, B., Agangi, A., Barbieri, R., Franchi, F., Gasparotto, G., 2014. The formation of low-temperature sedimentary pyrite and its relationship with biologically induced processes. *Geol. Ore Depos.* 56, 395-408.
- Ceramicola, S., Praeg, D., Cova, A., Accettella, D., Zecchin, M., 2014. Seafloor distribution and last glacial to postglacial activity of mud volcanoes on the Calabrian accretionary prism, Ionian Sea. *Geo-Marine Lett.* 34, 111-129. doi:10.1007/s00367-013-0354-y

1 Chafetz, H.S., Buczynski, C., 1992. Bacterially induced lithification of microbial mats.

2 Palaios 7, 277-293.

3
4
5 Chiodini, G., Marini, L., Russo, M., 2001. Geochemical evidence for the existence of high-

6 temperature hydrothermal brines at Vesuvio volcano, Italy. *Geochim. Cosmochim.*

7
8
9
10 Acta 65, 2129-2147

11
12 Clayton, R.N., Epstein, S., 1961. The use of oxygen isotopes in high-temperature geological

13 thermometry. *J. Geol.* 69, 447-452.

14
15
16 Cocker, J.D., Griffin, B.J., Muehlenbachs, K., 1982. Oxygen and carbon isotope evidence for

17 seawater-hydrothermal alteration of Macquarie Island ophiolite. *Earth Plan. Sci. Lett.*

18
19
20
21
22
23
24
25
26
27
28
29
30
31
32
33
34
35
36
37
38
39
40
41
42
43
44
45
46
47
48
49
50
51
52
53
54
55
56
57
58
59
60
61
62
63
64
65

60, 112-122.

CRC, 2005. *Handbook of Chemistry and Physics*, David R. Lide (ed.), Section 14, Geophys-

ics, Astronomy, and Acoustics; Abundance of Elements in the Earth's Crust and in the

Sea. 85th Edition, CRC Press. Boca Raton, Florida

Curtis, C.D., Coleman, M.L., 1986. Controls on the precipitation of early diagenetic calcite,

dolomite, and siderite concretions in complex depositional sequences. In: Gautier,

D.L. [Ed.], *Roles of organic matter in sediment diagenesis*: Society of Economic

Paleontologists and Mineralogists Special Publication 38, 23-33.

Curtis, C.D., Petrowski, C., Ortel, G., 1972. Stable carbon isotope ratios within carbonate

concretions: a clue to place and time of formation. *Nature* 235, 98-100.

Dählmann, A., de Lange, G.J., 2003. Fluid–sediment interactions at Eastern Mediterranean

mud volcanoes: a stable isotope study from ODP Leg 160. *Earth Planet. Sci. Lett.*

212, 377-391.

- 1
2
3
4
5
6
7
8 Dalla Valle, G., Gamberi, F., 2011. Pockmarks and seafloor instability in the Olbia continen-
9 tal slope (northeastern Sardinian margin, Tyrrhenian Sea). *Mar. Geophys. Res.* 32,
10 193-205.
11
12 Elderfield, H., Upstill-Goddard, R., Sholkovitz, E.R., 1990. The rare earth elements in rivers,
13 estuaries and coastal sea waters: processes affecting crustal input of elements to the
14 ocean and their significance to the composition of sea water. *Geochim. Cosmochim.*
15 *Acta* 54, 971-991.
16
17
18 Faccenna, C., Molin, P., Orecchio, B., Olivetti, V., Bellier, O., Funicello, F., Minelli, L.,
19 Piromallo, C., Billi, A., 2011. Topography of the Calabria subduction zone (southern
20 Italy): clues for the origin of Mt. Etna. *Tectonics*, 30 TC1003.
21
22
23
24
25
26
27 Feng, D., Chen, D., Peckmann, J., 2009. Rare earth elements in seep carbonates as tracers of
28 variable redox conditions at ancient hydrocarbon seeps. *Terra Nova* 21, 49-56.
29
30
31
32
33 Fernandez, A., van Dijk, J., Müller, I.A., Bernasconi, S.M., 2016. Siderite acid fractionation
34 factors for sealed and open vessel digestions at 70°C and 100°C. *Chem. Geol.* 444,
35 180-186.
36
37
38
39
40
41 Franchi, F., Hofmann, A., Cavalazzi, B., Wilson, A., Barbieri, R., 2015. Differentiating ma-
42 rine vs hydrothermal processes in Devonian carbonate mounds using rare earth ele-
43 ments (Kess Kess mounds, Anti-Atlas, Morocco). *Chem. Geol.* 409, 69-86.
44
45
46
47
48
49 Franchi, F., Turetta, C., Cavalazzi, B., Corami, F., Barbieri, R., 2016. Trace elements and
50 REE geochemistry of Middle Devonian carbonate mounds (Maïder Basin, Eastern
51 Anti-Atlas, Morocco): Implications for early diagenetic processes. *Sed. Geol.* 343, 56-
52 71.
53
54
55
56
57
58
59
60
61
62
63
64
65

- 1
2
3
4
5
6
7
8
9
10
11
12
13
14
15
16
17
18
19
20
21
22
23
24
25
26
27
28
29
30
31
32
33
34
35
36
37
38
39
40
41
42
43
44
45
46
47
48
49
50
51
52
53
54
55
56
57
58
59
60
61
62
63
64
65
- Fritz, P., Smith, D.G.W., 1970. The isotopic composition of secondary dolomites. *Geochim. Cosmochim. Acta* 34, 1161-1173.
- Fritz, P., Binda, P.L., Folinsbee, F.E., Krouse, H.R., 1971. Isotopic composition of diagenetic siderites from Cretaceous sediments in Western Canada. *J. Sediment. Petrol.* 41, 282-288.
- Gamberi, F., Rovere, M., 2010. Mud diapirs, mud volcanoes and fluid flowing: the rear of the Calabrian Arc Orogenic Wedge (southeastern Tyrrhenian Sea). *Basin Res.* 22, 452-464.
- Geletti, R., Del Ben, A., Buseti, M., Ramella, R., Volpi, V., 2008. Gas seeps linked to salt structures in the central Adriatic Sea. *Basin Res.* 20, 473-487. doi:10.1111/j.1365-2117.2008.00373.x
- German, C.R., Elderfield, H., 1990. Application of the Ce anomaly as a paleoredox indicator: the ground rules. *Paleoceanography* 5, 823-833.
- Goldstein, S.J., Jacobsen, S.B., 1988. Rare earth elements in river waters. *Earth Planet. Sci. Lett.* 89, 35-47.
- Gutscher, M.-A., Dominguez, S., de Lepinay, B.M., Pinheiro, L., Gallais, F., Babonneau, N., Cattaneo, A., Le Faou, Y., Barreca, G., Micallef, A., Rovere, M., 2015. Tectonic expression of an active slab tear from high-resolution seismic and bathymetric data offshore Sicily (Ionian Sea). *Tectonics* 34, doi:10.1002/2015TC003898.
- Haley, B.A., Klinkhammer, G.P., McManus, J., 2004. Rare earth elements in pore waters of marine sediments. *Geochim. Cosmochim. Acta* 68, 1265-1279.

- 1
2
3
4
5
6
7
8
9
10
11
12
13
14
15
16
17
18
19
20
21
22
23
24
25
26
27
28
29
30
31
32
33
34
35
36
37
38
39
40
41
42
43
44
45
46
47
48
49
50
51
52
53
54
55
56
57
58
59
60
61
62
63
64
65
- Hein, J.R., Normark, W.R., McIntyre, B.R., Lorenson, T.D., Powell II, C.L., 2006. Methanogenic calcite, ¹³C-depleted bivalve shells, and gas hydrate from a mud volcano offshore southern California. *Geology* 34, 109-112.
- Helz, G.R., Miller, C.V., Charnock, J.M., Mosselmans, J.F.W., Patrick, R.A.D., Garner, C.D., Vaughan, D.J., 1996. Mechanism of molybdenum removal from the sea and its concentration in black shales: EXAFS evidence. *Geochim. Cosmochim. Acta* 60, 3631-3642.
- Hicks, K.S., Compton, J.S., McCracken, S., Vecsei, A., 1996. Origin of diagenetic carbonate minerals recovered from the New Jersey continental slope. *In: Mountain, G.S., Miller, K.G., Blum, P., Poag, C.W., Twichell, D.C. [Eds.] Proc. ODP, Sci. Results, 150: College Station, TX (Ocean Drilling Program)*, 311-323.
- Himmler, T., Bach, W., Bohrmann, G., Peckmann, J., 2010. Rare earth elements in authigenic methane-seep carbonates as tracers for fluid composition during early diagenesis. *Chem. Geol.* 277, 126-136.
- Hovland, M., Gardner, J.V., Judd, A.G., 2002. The significance of pockmarks to understanding fluid flow processes and geohazards. *Geofluids* 2, 127-136. doi:10.1046/j.1468-8123.2002.00028.x
- Hu, Y., Feng, D., Peckmann, J., Roberts, H.H., Chen, D., 2014. New insights into cerium anomalies and mechanisms of trace metal enrichment in authigenic carbonate from hydrocarbon seeps. *Chem. Geol.* 381, 55-66.
- Irwin, H., Curtis, C.D., Coleman, M., 1977. Isotopic evidence for source of diagenetic carbonates formed during burial of organic-rich sediments. *Nature* 269, 209-213.

- 1
2
3
4
5
6
7
8
9
10
11
12
13
14
15
16
17
18
19
20
21
22
23
24
25
26
27
28
29
30
31
32
33
34
35
36
37
38
39
40
41
42
43
44
45
46
47
48
49
50
51
52
53
54
55
56
57
58
59
60
61
62
63
64
65
- Jimenez-Lopez, C., Romanek, C.S., 2004. Precipitation kinetics and carbon isotope partitioning of inorganic siderite at 25°C and 1 atm. *Geochim. Cosmochim. Acta* 68, 557-571.
- Kamber, B.S., Bolhar, R., Webb, G.E., 2004. Geochemistry of late Archaean stromatolites from Zimbabwe; evidence for microbial life in restricted epicontinental seas. *Precambrian Res.* 132, 379-399.
- Kim, S.-T., O'Neil, J.R., 1997. Equilibrium and nonequilibrium oxygen isotope effects in synthetic carbonates. *Geochim. Cosmochim. Acta* 61, 3461-3475.
- Kim, S.-T., O'Neil, J.R., Hillaire-Marcel, C., Mucci, A., 2007. Oxygen isotope fractionation between synthetic aragonite and water: Influence of temperature and Mg^{2+} concentration. *Geochim. Cosmochim. Acta* 71, 4704-4715.
- Kim, J.-H., Torres, M.E., Haley, B.A., Kastner, M., Pohlman, J.W., Riedel, M., Lee, Y.-J., 2012. The effect of diagenesis and fluidmigration on rare earth element distribution in pore fluids of the northern Cascadia accretionary margin. *Chem. Geol.* 291, 152-165.
- Klinkhammer, G.P., Elderfield, H., Edmond, J.M., Mitra, A., 1994. Geochemical implications of rare earth element patterns in hydrothermal fluids from mid-ocean ridges. *Geochim. Cosmochim. Acta* 58, 5105-5113.
- Krastel, S., Spiess, V., Ivanov, M., Weinrebe, W., Bohrmann, G., Shashkin, P., Heidersdorf, F., 2003. Acoustic investigations of mud volcanoes in the Sorokin Trough, Black Sea. *Geo-Marine Lett.* 23, 230-238. doi:10.1007/s00367-003-0143-0
- Lawrence, M.G., Greig, A., Collerson, K.D., Kamber, B.S., 2006. Rare Earth Element and Yttrium Variability in South East Queensland Waterways. *Aquat. Geochem.* 12, 39-72.

- 1
2
3
4
5
6
7
8
9
10
11
12
13
14
15
16
17
18
19
20
21
22
23
24
25
26
27
28
29
30
31
32
33
34
35
36
37
38
39
40
41
42
43
44
45
46
47
48
49
50
51
52
53
54
55
56
57
58
59
60
61
62
63
64
65
- Lécuyer, C., Fourcade, S., 1991. Oxygen isotope evidence for multi-stage hydrothermal alteration at a fossil slow-spreading center: The Silurian Trinity ophiolite (California, U.S.A.). *Chem. Geol.* 87, 231-246.
- Lécuyer, C., Allemand, P., 1999. Modelling of the oxygen isotope evolution of seawater: Implications for the climate interpretation of the $\delta^{18}\text{O}$ of marine sediments. *Geochim. Cosmochim. Acta* 63, 351-361.
- Levin, L.A., Mendoza, G.F., Grupe, B.M., 2016. Methane seepage effects on biodiversity and biological traits of macrofauna inhabiting authigenic carbonates. *Deep Sea Res. Part II Top. Stud. Oceanogr.* 1-16. doi:10.1016/j.dsr2.2016.05.021
- Lietard, C., Pierre, C., 2009. Isotopic signatures ($\delta^{18}\text{O}$ and $\delta^{13}\text{C}$) of bivalve shells from cold seeps and hydrothermal vents. *Geobios* 42, 209-219.
- Løseth, H., Gading, M., Wensaas, L., 2009. Hydrocarbon leakage interpreted on seismic data. *Mar. Pet. Geol.* 26, 1304-1319. doi:10.1016/j.marpetgeo.2008.09.008
- Maekawa, T., 2004, Experimental study on isotopic fractionation in water during gas hydrate formation. *Geochem. J.* 38, 129-138.
- Magalhães, V.H., Pinheiro, L.M., Ivanov, M.K., Kozlova, E., Blinova, V., Kolganova, J., Vasconcelos, C., McKenzie, J.A., Bernasconi, S.M., Kopf, A.J., Díaz-del-Río, V., González, F.J., Somoza, L., 2012. Formation processes of methane-derived authigenic carbonates from the Gulf of Cadiz. *Sediment. Geol.* 243-244, 155-168.
- Masclé, J., Mary, F., Praeg, D., Brosolo, L., Camera, L., Ceramicola, S., Dupré, S., 2014. Distribution and geological control of mud volcanoes and other fluid/free gas seepage features in the Mediterranean Sea and nearby Gulf of Cadiz. *Geo-Mar. Lett.* 34, 89-110. doi:10.1007/s00367-014-0356-4

- 1
2
3
4
5
6
7
8
9
10
11
12
13
14
15
16
17
18
19
20
21
22
23
24
25
26
27
28
29
30
31
32
33
34
35
36
37
38
39
40
41
42
43
44
45
46
47
48
49
50
51
52
53
54
55
56
57
58
59
60
61
62
63
64
65
- Matsumoto, R., 1989. Isotopically heavy oxygen-containing siderite derived from the decomposition of methane hydrate. *Geology* 17, 707-710.
- Mazzini, A., Aloisi, G., Akhmanov, G.G., Parnell, J., Cronin, B.T., Murphy, P., 2005. Integrated petrographic and geochemical record of hydrocarbon seepage on the Vøring Plateau. *J. Geol. Soc. Lond.* 162, 815-827.
- Micallef, A., Berndt, C., Debono, G., 2011. Fluid flow systems of the Malta Plateau, Central Mediterranean Sea. *Mar. Geol.* 284, 74-85. doi:10.1016/j.margeo.2011.03.009
- Milia, A., Turco, E., Pierantoni, P.P., Schettino, A., 2009. Four-dimensional tectonostratigraphic evolution of the Southeastern peri-Tyrrhenian basins (margin of Calabria, Italy). *Tectonophysics* 476, 41-56.
- Minissale, A., Magro, G., Vaselli, O., Verrucchi, C., Perticone, I., 1997. Geochemistry of water and gas discharges from the Mt. Amiata silicic complex and surrounding areas (central Italy). *J. Vulcanol. Geotherm. Res.* 79, 223-251.
- Monty, C.L.V., 1995. The rise and nature of carbonate mudmounds: an introductory actualistic approach. In: Monty, C.L.V., Bosence, D.W.J., Bridges, P.H., Pratt, B.R. (Eds.), *Carbonate Mud-Mounds, Their Origin and Evolution*. Spec. Publ. Int. Assoc. Sedimentol. 23. Blackwell, Oxford, pp. 11-48.
- Mozley, P.S., Wersin, P., 1992. Isotopic composition of siderite as an indicator of depositional environment. *Geology* 20, 817-820.
- Muehlenbachs, K., Hodges, F.N., 1978. Oxygen isotope geochemistry of rocks from DSDP LEG 46. In: *Reps. DSDP 46*, 257-259.

- 1 Murray, R.W., Buchholtz ten Brink, M.R., Gerlach, D.C., Price Russ III, G., Jones, D.L.,
2 1991. Rare earth, major, and trace elements in chert from the Franciscan Complex and
3 Monterey Group, California: assessing sources to fine-grained marine sediments.
4
5 Geochim. Cosmochim. Acta 55, 1875-1895.
6
7
8
9
10 Neubert, N., Nagler, T.F., Böettcher, M.E., 2008. Sulfidity controls molybdenum isotope
11 fractionation into euxinic sediments: evidence from the modern Black Sea. *Geology*
12 36, 775-778.
13
14
15
16
17
18 Nothdurft, L.D., Webb, G.E., Kamber, B.S., 2004. Rare earth element geochemistry of Late
19 Devonian reefal carbonates, Canning Basin, Western Australia: confirmation of a
20 seawater REE proxy in ancient limestones. *Geochim. Cosmochim. Acta* 68, 263-283.
21
22
23
24
25
26
27 Nozaki, Y., Zhang, J., Amakawa, H., 1997. The fractionation between Y and Ho in the ma-
28 rine environment. *Earth Planet. Sci. Lett.* 148, 329-340.
29
30
31
32
33 Olivier, N., Boyet, M., 2006. Rare earth and trace elements of microbialites in Upper Jurassic
34 coral- and sponge-microbialite reefs. *Chem. Geol.* 230, 105-123.
35
36
37
38
39 Pack, A., Russell, S.S., Michael, J., Shelley, G., van Zuilen, M., 2007. Geo- and
40 cosmochemistry of the twin elements yttrium and holmium. *Geochim. Cosmochim.*
41 *Acta* 71, 4592-4608.
42
43
44
45
46
47 Paonita, A., Favara, R., Nuccio, P.M., Sortino, F., 2002. Genesis of fumarolic emissions as
48 inferred by isotope mass balances: CO₂ and water at Vulcano Island, Italy. *Geochim.*
49 *Cosmochim. Acta*, 66, 759-772.
50
51
52
53
54
55 Passaro, S., Tamburrino, S., Vallefucio, M., Tassi, F., Vaselli, O., Giannini, L., Chiodini, L.,
56 Caliro, S., Sacchi, M., Rizzo, A.L., Ventura, G., 2016. Seafloor doming driven by
57
58
59
60
61
62
63
64
65

1 degassing processes unveils sprouting volcanism in coastal areas. *Sci. Rep.* 6, 22448.

2 doi: 10.1038/srep22448.

3
4
5 Peckmann, J., Reimer, A., Luth, U., Luth, C., Hansen, B.T., Heinicke, C., Hoefs, J., Reitner,
6
7
8 J., 2001. Methane-derived carbonates and authigenic pyrite from the northwestern
9
10 Black Sea. *Mar. Geol.* 177, 129-150.

11
12
13 Peckmann, J., Birgel, D., Kiel, S., 2009. Molecular fossils reveal fluid composition and flow
14
15 intensity at a Cretaceous seep. *Geology* 37, 847-850.

16
17
18 Peckmann, J., Thiel, V., 2004. Carbon cycling at ancient methane-seeps. *Chem. Geol.* 205,
19
20
21 443-467.

22
23
24
25 Peters, M., Strauss, H., Petersen, S., Kummer, N.A., Thomazo, C., 2011. Hydrothermalism in
26
27 the Tyrrhenian Sea: Inorganic and microbial sulfur cycling as revealed by geochemi-
28
29 cal and multiple sulfur isotope data. *Chem. Geol.* 280, 217-231.
30
31
32 doi:10.1016/j.chemgeo.2010.11.011

33
34
35
36 Pourret, O., Davranche, M., Gruau, G., Dia, A., 2008. New insights into cerium anomalies in
37
38 organic-rich alkaline waters. *Chem. Geol.* 251, 120-127.

39
40
41 Reynard, B., Lécuyer, C., Grandjean, P., 1999. Crystal-chemical controls on rare earth ele-
42
43 ment concentrations in fossil biogenic apatite and implications for
44
45 paleoenvironmental reconstructions. *Chem. Geol.* 155, 233-242.

46
47
48
49 Rongemaille, E., Bayon, G., Pierre, C., Bollinger, C., Chu, N.C., Fouquet, Y., Riboulot, V.,
50
51
52 Voisset, M., 2011. Rare earth elements in cold seep carbonates from the Niger delta.
53
54
55
56
57
58
59
60
61
62
63
64
65
66
67
68
69
70
71
72
73
74
75
76
77
78
79
80
81
82
83
84
85
86
87
88
89
90
91
92
93
94
95
96
97
98
99
100
101
102
103
104
105
106
107
108
109
110
111
112
113
114
115
116
117
118
119
120
121
122
123
124
125
126
127
128
129
130
131
132
133
134
135
136
137
138
139
140
141
142
143
144
145
146
147
148
149
150
151
152
153
154
155
156
157
158
159
160
161
162
163
164
165
166
167
168
169
170
171
172
173
174
175
176
177
178
179
180
181
182
183
184
185
186
187
188
189
190
191
192
193
194
195
196
197
198
199
200
201
202
203
204
205
206
207
208
209
210
211
212
213
214
215
216
217
218
219
220
221
222
223
224
225
226
227
228
229
230
231
232
233
234
235
236
237
238
239
240
241
242
243
244
245
246
247
248
249
250
251
252
253
254
255
256
257
258
259
260
261
262
263
264
265
266
267
268
269
270
271
272
273
274
275
276
277
278
279
280
281
282
283
284
285
286
287
288
289
290
291
292
293
294
295
296
297
298
299
300
301
302
303
304
305
306
307
308
309
310
311
312
313
314
315
316
317
318
319
320
321
322
323
324
325
326
327
328
329
330
331
332
333
334
335
336
337
338
339
340
341
342
343
344
345
346
347
348
349
350
351
352
353
354
355
356
357
358
359
360
361
362
363
364
365
366
367
368
369
370
371
372
373
374
375
376
377
378
379
380
381
382
383
384
385
386
387
388
389
390
391
392
393
394
395
396
397
398
399
400
401
402
403
404
405
406
407
408
409
410
411
412
413
414
415
416
417
418
419
420
421
422
423
424
425
426
427
428
429
430
431
432
433
434
435
436
437
438
439
440
441
442
443
444
445
446
447
448
449
450
451
452
453
454
455
456
457
458
459
460
461
462
463
464
465
466
467
468
469
470
471
472
473
474
475
476
477
478
479
480
481
482
483
484
485
486
487
488
489
490
491
492
493
494
495
496
497
498
499
500
501
502
503
504
505
506
507
508
509
510
511
512
513
514
515
516
517
518
519
520
521
522
523
524
525
526
527
528
529
530
531
532
533
534
535
536
537
538
539
540
541
542
543
544
545
546
547
548
549
550
551
552
553
554
555
556
557
558
559
560
561
562
563
564
565
566
567
568
569
570
571
572
573
574
575
576
577
578
579
580
581
582
583
584
585
586
587
588
589
590
591
592
593
594
595
596
597
598
599
600
601
602
603
604
605
606
607
608
609
610
611
612
613
614
615
616
617
618
619
620
621
622
623
624
625
626
627
628
629
630
631
632
633
634
635
636
637
638
639
640
641
642
643
644
645
646
647
648
649
650
651
652
653
654
655
656
657
658
659
660
661
662
663
664
665
666
667
668
669
670
671
672
673
674
675
676
677
678
679
680
681
682
683
684
685
686
687
688
689
690
691
692
693
694
695
696
697
698
699
700
701
702
703
704
705
706
707
708
709
710
711
712
713
714
715
716
717
718
719
720
721
722
723
724
725
726
727
728
729
730
731
732
733
734
735
736
737
738
739
740
741
742
743
744
745
746
747
748
749
750
751
752
753
754
755
756
757
758
759
760
761
762
763
764
765
766
767
768
769
770
771
772
773
774
775
776
777
778
779
780
781
782
783
784
785
786
787
788
789
790
791
792
793
794
795
796
797
798
799
800
801
802
803
804
805
806
807
808
809
810
811
812
813
814
815
816
817
818
819
820
821
822
823
824
825
826
827
828
829
830
831
832
833
834
835
836
837
838
839
840
841
842
843
844
845
846
847
848
849
850
851
852
853
854
855
856
857
858
859
860
861
862
863
864
865
866
867
868
869
870
871
872
873
874
875
876
877
878
879
880
881
882
883
884
885
886
887
888
889
890
891
892
893
894
895
896
897
898
899
900
901
902
903
904
905
906
907
908
909
910
911
912
913
914
915
916
917
918
919
920
921
922
923
924
925
926
927
928
929
930
931
932
933
934
935
936
937
938
939
940
941
942
943
944
945
946
947
948
949
950
951
952
953
954
955
956
957
958
959
960
961
962
963
964
965
966
967
968
969
970
971
972
973
974
975
976
977
978
979
980
981
982
983
984
985
986
987
988
989
990
991
992
993
994
995
996
997
998
999
1000

- 1
2
3
4
5
6
7
8
9
10
11
12
13
14
15
16
17
18
19
20
21
22
23
24
25
26
27
28
29
30
31
32
33
34
35
36
37
38
39
40
41
42
43
44
45
46
47
48
49
50
51
52
53
54
55
56
57
58
59
60
61
62
63
64
65
- Rovere, M., Gamberi, F., Mercorella, A., Rashed, H., Gallerani, A., Leidi, E., Marani, M., Funari, V., Pini, G.A., 2014. Venting and seepage systems associated with mud volcanoes and mud diapirs in the southern Tyrrhenian Sea. *Mar. Geol.* 347, 153-171.
- Rovere, M., Rashed, H., Pecchioni, E., Mercorella, A., Ceregato, A., Leidi, E., Gamberi, F., Vaselli, O., 2015. Habitat mapping of cold seeps associated with authigenic mineralization (Paola Ridge, southern Tyrrhenian Sea): combining seafloor backscatter with biogeochemistry signals. *Ital. J. Geosci.* 134, 23-31.
- Sato, H., Hayashi, K.-i., Ogawa, Y., Kawamura, K., 2012. Geochemistry of deep sea sediments at cold seep sites in the Nankai Trough: insights into the effect of anaerobic oxidation of methane. *Mar. Geol.* 323-325, 47-55.
- Savini, A., Malinverno, E., Etiope, G., Tessarolo, C., Corselli, C., 2009. Shallow seep-related seafloor features along the Malta plateau (Sicily channel – Mediterranean Sea): Morphologies and geo-environmental control of their distribution. *Mar. Pet. Geol.* 26, 1831-1848. doi:10.1016/j.marpetgeo.2009.04.003
- Solomon, E.A., Kastner, M., Jannasch, H., Robertson, G., Weinstein, Y., 2008. Dynamic fluid flow and chemical fluxes associated with a seafloor gas hydrate deposit on the northern Gulf of Mexico slope. *Earth Planet. Sci. Lett.* 270, 95-105.
- Sommer, S., Schmidt, M., Linke, P., 2015. Continuous inline mapping of a dissolved methane plume at a blowout site in the Central North Sea UK using a membrane inlet mass spectrometer—Water column stratification impedes immediate methane release into the atmosphere. *J. Mar. Petrol. Geol.* 68, 766-775.
- Sultan, N., Bohrmann, G., Ruffine, L., Pape, T., Riboulot, V., Colliat, J.-L., Prunelé, A. De, Dennielou, B., Garziglia, S., Himmler, T., Marsset, T., Peters, C.A., Rabiou, A., Wei,

- 1 J., 2014. Pockmark formation and evolution in deep water Nigeria: Rapid hydrate
2 growth versus slow hydrate dissolution. *J. Geophys. Res. Solid Earth* 119, 2679-2694.
3
4 doi:10.1029/2010JB007453
5
6
7
8 Tang, J., Johannesson, K.H., 2003. Speciation of rare earth elements in natural terrestrial wa-
9
10 ters: assessing the role of dissolved organic matter from the modeling approach.
11
12 *Geochim. Cosmochim. Acta* 67, 2321-2339.
13
14
15
16 Taviani, M., 2001. Fluid venting and associated processes. *In: Vai, G.B., Maltini, I.P.* [Eds]
17
18 *Anatomy of an Orogen: The Apennines and Adjacent Mediterranean Basins*. Kluwer
19
20 Academic Publisher, Great Britain, pp. 351-366.
21
22
23
24 Taviani, M., Angeletti, L., Ceregato, A., Foglini, F., Frogli, C., Trincardi, F., 2013. The Gela
25
26 Basin pockmark field in the strait of Sicily (Mediterranean Sea): chemosymbiotic
27
28 faunal and carbonate signatures of postglacial to modern cold seepage.
29
30 *Biogeosciences* 10, 1-19.
31
32
33
34
35 Taviani, M., Franchi, F., Angeletti, L., Correggiari, A., López Correa, M., Maselli, V.,
36
37 Mazzoli, C., Peckmann, J., 2015. Biodepositional carbonates on the Adriatic continental
38
39 shelf imprinted by oxidation of seeping hydrocarbons. *J.Mar. Petrol. Geol.* 66, 511-
40
41 531.
42
43
44
45 Taylor, S.R., McLennan, S.M., 1985. *The Continental Crust: its Composition and Evolution*.
46
47 Blackwell Scientific Pub, Palo Alto, CA, 328 pp.
48
49
50
51 Taylor, K.G., Curtis, C.D., 1995. Stability and facies association of early diagenetic mineral
52
53 assemblages: an example from a Jurassic ironstone- mudstone succession, UK. *J. Sed-*
54
55 *iment. Petrol.* 65, 358-368.
56
57
58
59
60
61
62
63
64
65

- 1
2
3
4
5
6
7
8
9
10
11
12
13
14
15
16
17
18
19
20
21
22
23
24
25
26
27
28
29
30
31
32
33
34
35
36
37
38
39
40
41
42
43
44
45
46
47
48
49
50
51
52
53
54
55
56
57
58
59
60
61
62
63
64
65
- Tostevin, R., Shields, G.A., Tarbuck, G.M., He, T., Clarkson, M.O., Wood, R.A., 2016. Effective use of cerium anomalies as a redox proxy in carbonate-dominated marine settings. *Chem. Geol.* 438, 146-162.
- Vasconcelos, C., McKenzie, J.A., Warthmann, R., Bernasconi, S.M., 2005. Calibration of the $\delta^{18}\text{O}$ paleothermometer for dolomite precipitated in microbial cultures and natural environments. *Geology* 33, 317-320.
- Vaselli, O., Tassi, F., Montegrossi, G., Capaccioni, B., Giannini, L., 2006. Sampling and analysis of fumarolic gases. *Acta Vulcanol.*, 1-2, 65-76.
- Vaselli, O., Tassi, F., Tedesco, D., Poreda, J.R., Caprai, A., 2011. Submarine and inland gas discharges from the Campi Flegrei (southern Italy) and the Pozzuoli Bay: geochemical clues for a common hydrothermal-magmatic source. Special Volume on "Research in Shallow Marine and Fresh Water Systems", *Procedia Earth Planet. Sci.*, 4, 57-73.
- Vergnaud-Grazzini, C., 1971. ^{18}O changes in foraminiferal carbonates during the last 105 years in the Mediterranean Sea. *Mar. Geol.* 11, 261-282.
- Viola, I., Oppo, D., Franchi, F., Capozzi, R., Dinelli, E., Liverani, B., Taviani, M., 2015. Mineralogy, geochemistry and petrography of methane-derived authigenic carbonates from Enza River, Northern Apennines (Italy). *Mar. Pet. Geol.* 66, 566-581.
- Von Deimling, J.S., Linke, P., Schmidt, M., Rehder, G., 2015. Ongoing methane discharge at well site 22/4b (NorthSea) and discovery of a spiral vortex bubble plume motion. *J. Mar. Petrol. Geol.* 68, 618-630.
- Webb, G.E., Kamber, B.S., 2000. Rare earth elements in Holocene reefal microbialites: a new shallow seawater proxy. *Geochim. Cosmochim. Acta* 64, 1557-1565.

- 1
2
3
4
5
6
7
8
9
10
11
12
13
14
15
16
17
18
19
20
21
22
23
24
25
26
27
28
29
30
31
32
33
34
35
36
37
38
39
40
41
42
43
44
45
46
47
48
49
50
51
52
53
54
55
56
57
58
59
60
61
62
63
64
65
- Whiticar, M.J., 1999. Carbon and hydrogen isotope systematics of bacterial formation and oxidation of methane. *Chem. Geol.* 161, 291-314.
- Wittkop, C., Teranes, J., Lubenow, B., Dean, W.E., 2014. Carbon- and oxygen-stable isotopic signatures of methanogenesis, temperature, and water column stratification in Holocene siderite varves. *Chem. Geol.* 389, 153-166.
- Zhang, J., Nozaki, Y., 1996. Rare earth elements and yttrium in seawater: ICP-MS determinations in the East Caroline, Coral Sea, and South Fiji basins of the western South Pacific Ocean. *Geochim. Cosmochim. Acta* 60, 4631-4644.
- Zhang, J., Nozaki, Y., 1998. Behavior of rare earth elements in seawater at the ocean margin: A study along the slopes of the Sagami and Nankai troughs near Japan. *Geochim. Cosmochim. Acta* 62, 1307-1317.
- Zhang, J., Amakawa, H., Nozaki, Y., 1994. The comparative behaviors of yttrium and lanthanides in seawater of the North Pacific. *Geophys. Res. Lett.* 21, 2677-2680.
- Zhang, F., Xu, H., Konishi, H., Kemp, J.M., Roden, E.E., Shen, Z., 2012. Dissolved sulfide-catalyzed precipitation of disordered dolomite: implications for the formation mechanism of sedimentary dolomite. *Geochim. Cosmochim. Acta* 97, 148-165.
- Zhong, S., Mucci, A., 1995. Partitioning of rare earth elements (REEs) between calcite and seawater solutions at 25°C and 1 atm, and high dissolved REE concentrations. *Geochim. Cosmochim. Acta* 59, 443-453.

TABLE AND FIGURE CAPTIONS

Table 1. Sampling stations (Fig. 1), depth and description of the samples (sediments, concretions, water and gas). Mineralogical and stable isotope composition of limestone and siderite samples is also provided. Data from Rovere et al. (2015) are highlighted in gray.

Table 2. Major oxides (wt. %) and trace elements (ppm) composition of calcite/aragonite concretions from the Paola Ridge.

Table 3. Major oxides (wt. %) and trace elements (ppm) composition of siderites from the Paola Ridge. In gray, the chemical composition measured in a second laboratory (see text for further explanations).

Table 4. Major oxides (wt. %) and trace elements (ppm) composition of sulfides from the Paola Ridge.

Table 5. Major oxides (wt. %) and trace elements (ppm) composition of Fe-oxy-hydroxides from the Paola Ridge.

Table 6. Major oxides (wt. %) and trace elements (ppm) composition of muddy sediments from the Paola Ridge.

1 **Table 7.** Chemical composition (in % by vol.) and $\delta^{13}\text{C-CO}_2$ and $\delta^{18}\text{O-CO}_2$ V-PDB values of
2 the venting gases.
3
4
5
6
7
8

9 **Table 8.** Chemical composition of the seawater recovered by rosette samplers. Total alkalini-
10 ty and ion contents are in mg L^{-1} while free- CO_2 is in mmol L^{-1} .
11
12
13
14
15
16
17

18 **Figure 1.** Bathymetry of the Paola Ridge area. The dotted blue lines outline the pockmark-
19 punctuated mud diapirs (D1, D2 and D3) and the alleged mud volcanoes R1MV and RMV
20 (Rovere et al., 2014). See Table 1 for samples description. Inset: subduction system of the
21 central Mediterranean area with location and depth of the subduction slab projected over the
22 study area (box).
23
24
25
26
27
28
29
30
31
32
33

34 **Figure 2.** Simplified lithostratigraphy and magnetic susceptibility of the drill cores from
35 which all the carbonate, sulfide, Fe-oxy-hydroxide and mud samples were collected for this
36 study. Magnetic susceptibility is in S.I. $\times 10^6$. Some of the samples, listed in Table 1, are also
37 outlined along the core logs. All the cores displayed in the figure were collected during the
38 MVP11 cruise.
39
40
41
42
43
44
45
46
47
48
49
50

51 **Figure 3.** Carbonate concretions: **A)** Aragonite/calcite concretion (Sample Cal-N). **B)** Sider-
52 ite crust (Sample Cal-E). **C)** Section of a siderite tubular concretion (Sample Cal-MB4). **D)**
53 Siderite tubular concretion (Sample Cal-G) showing the typical whitish outer crust.
54
55
56
57
58
59
60
61
62
63
64
65

1 **Figure 4.** Transmitted light photomicrographs of the carbonate concretions. **A)** Cal-
2 cite/aragonite concretion with foraminifera remains and abundant terrigenous material. **B)**
3
4 Transversal section of sample Cal-G showing concentric layering of the concretion; outer
5 part is toward the top of the figure. The bulk of the concretion is micro- to meso-sparitic si-
6 derite. **C)** Interlocking crystals of siderite with a turbid core (white arrow) in sample Cal-FF.
7
8
9
10
11
12 A: cross-polarized light; B-C: plane-polarized light.
13
14
15
16
17

18 **Figure 5.** Sulfide crusts in the Cal-O sample (**A**) and sulfide tubular concretions in sample
19 Cal-Q (**B**).
20
21
22
23
24
25
26

27 **Figure 6.** Reflected light photomicrographs of the sulfide concretions (Sample Cal-S). **A)**
28 Crustiform sulfides (pyrite/marcasite). The dark area on the left of the figure is primary po-
29 rosity. **B-C)** Aggregate of anhedral and granular sulfides (pyrite/marcasite), respectively.
30
31
32
33
34
35
36
37
38

39 **Figure 7.** PAAS-normalized REE patterns of calcite/aragonite (**A**), sulfides (**B**), Fe-oxy-
40 hydroxides (**C**) and muddy sediments (**D**).
41
42
43
44
45
46
47

48 **Figure 8.** PAAS-normalized REE patterns of siderite concretions (* refers to the second se-
49 ries of analyses, see table 3).
50
51
52
53
54
55
56

57 **Figure 9.** Binary diagrams of terrigenous contaminant proxies versus Σ REE, LREE and
58 Y/Ho for the calcite/aragonite and siderite concretions.
59
60
61
62
63
64
65

1
2
3 **Figure 10.** A) Hypothetical mixing trend of average REE composition of calcite/aragonite
4 and Fe-oxy-hydroxides. B) Hypothetical mixing trend of average REE composition of sider-
5
6 ite (without sample Cal-MB4) and Fe-oxy-hydroxides.
7
8
9

10
11
12
13
14 **Supplementary Material S1.** Trace element distributions within the studied samples.
15
16
17
18
19
20
21
22
23
24
25
26
27
28
29
30
31
32
33
34
35
36
37
38
39
40
41
42
43
44
45
46
47
48
49
50
51
52
53
54
55
56
57
58
59
60
61
62
63
64
65

Figure 1
[Click here to download high resolution image](#)

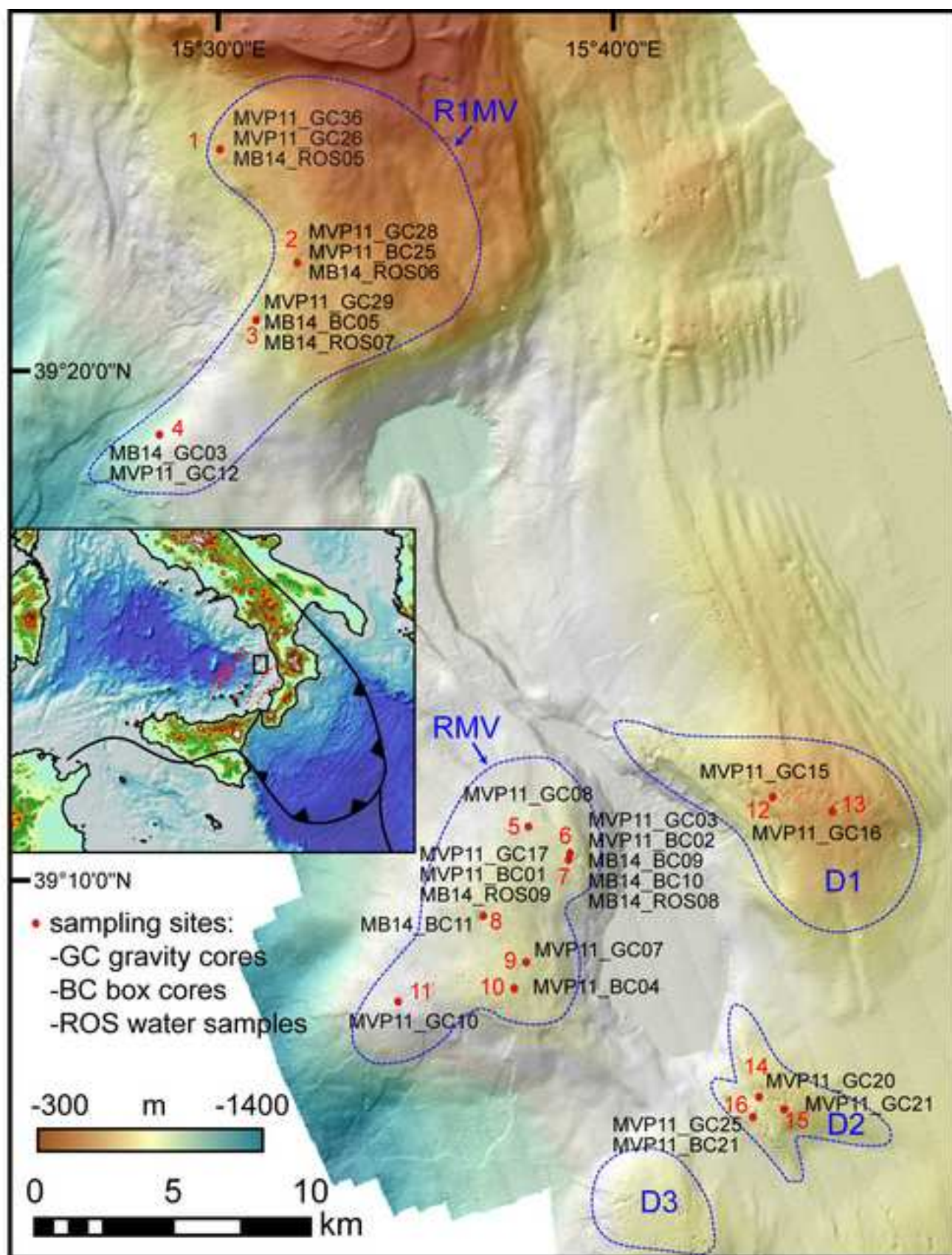


Fig. 1

Figure 2
[Click here to download high resolution image](#)

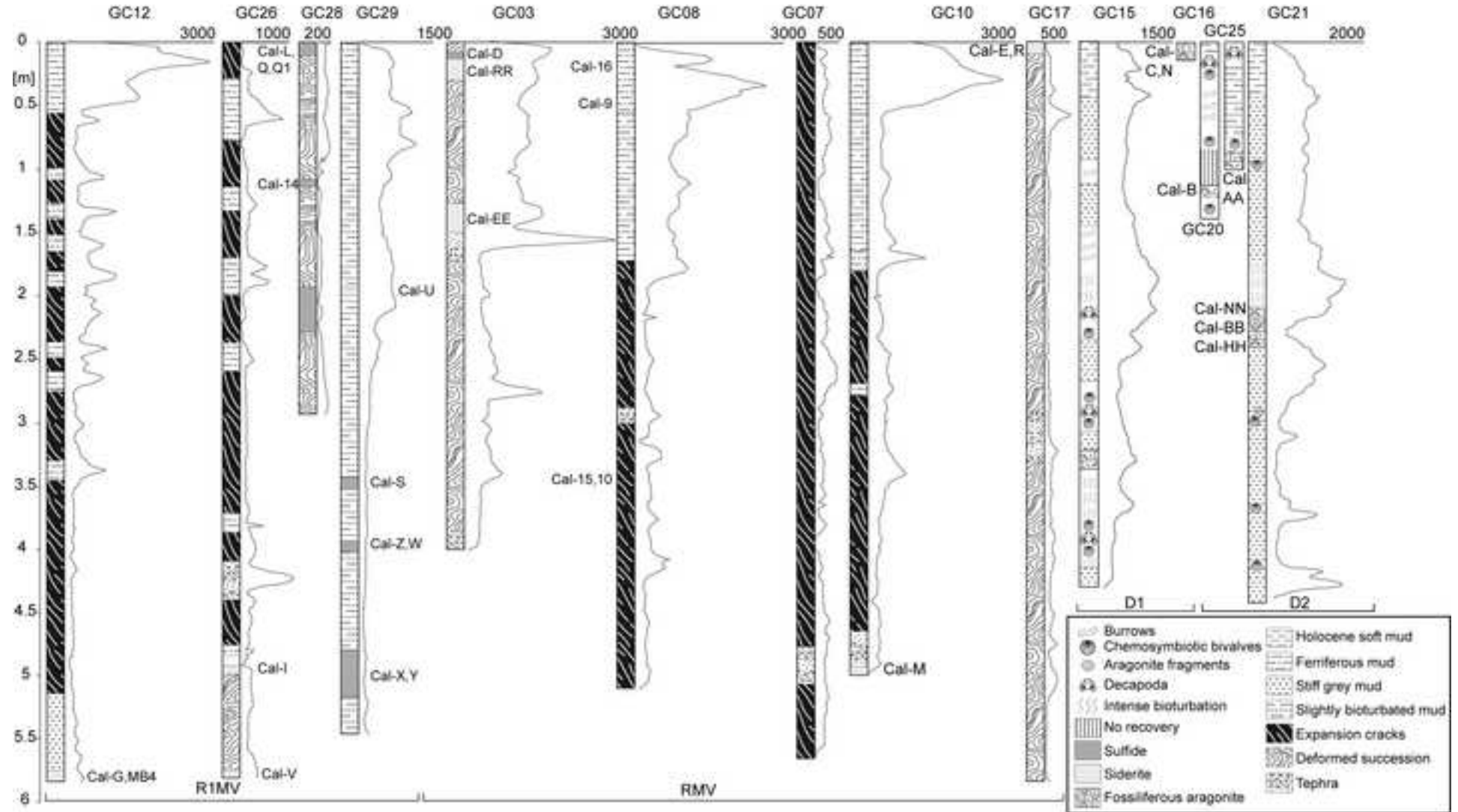


Fig. 2

Figure 3
[Click here to download high resolution image](#)



Fig. 3

Figure 4
[Click here to download high resolution image](#)

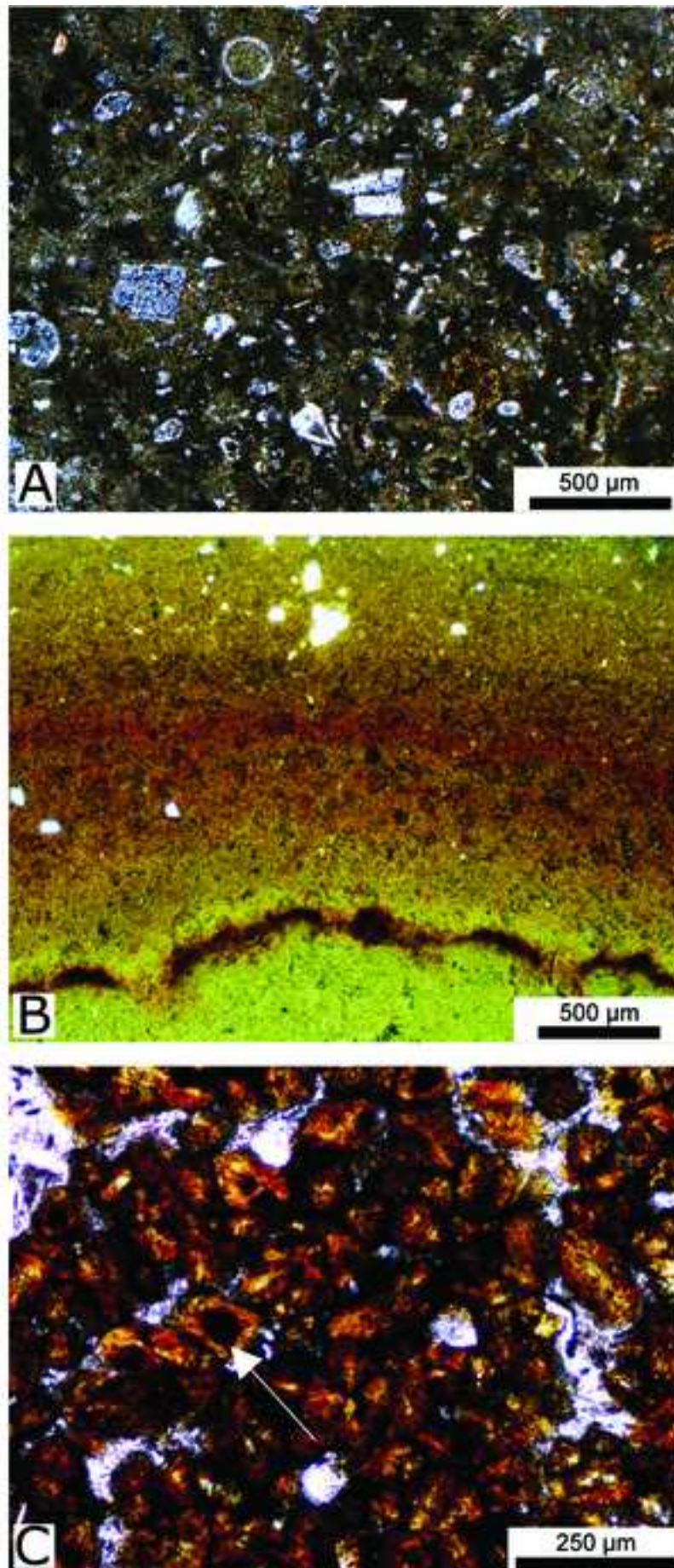


Fig. 4

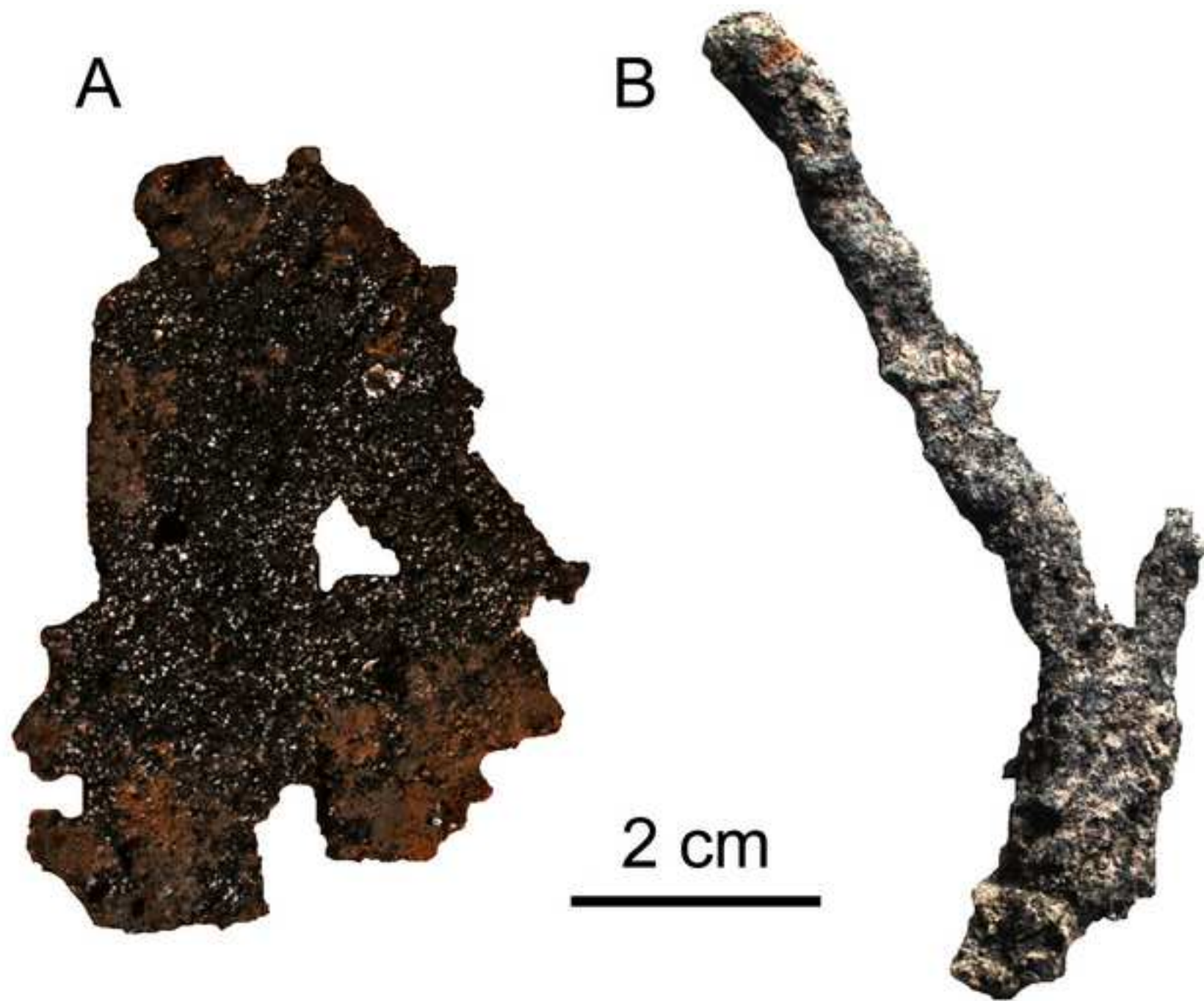


Fig. 5

Figure 6
[Click here to download high resolution image](#)

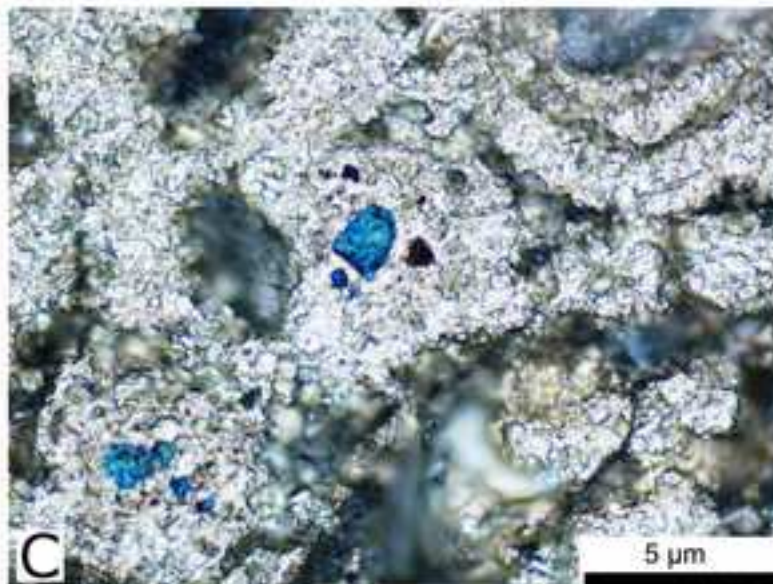
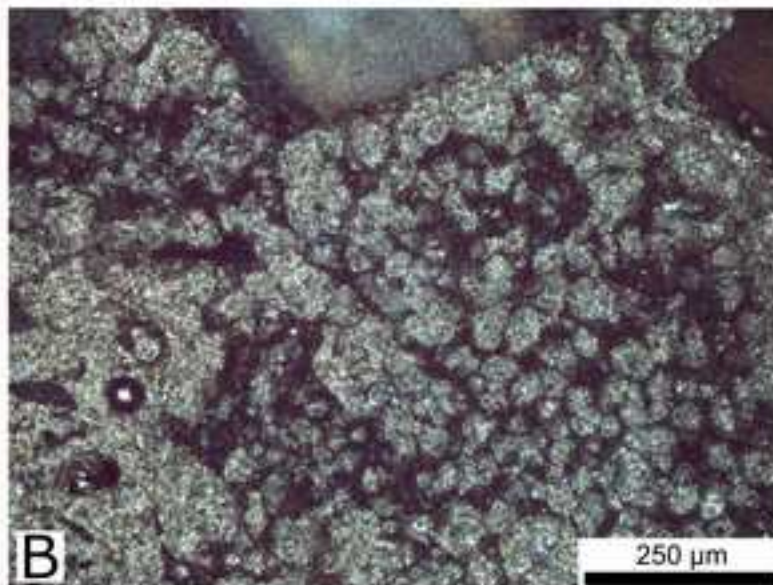
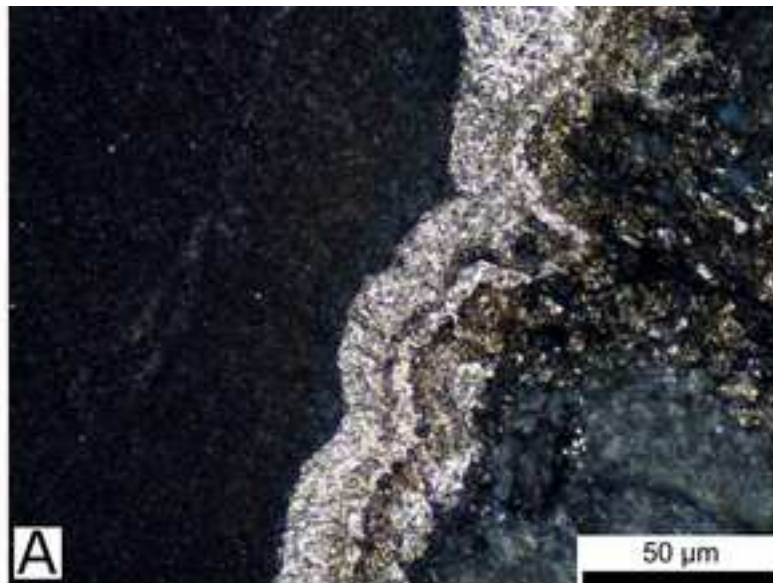


Fig. 6

Figure 7
[Click here to download high resolution image](#)

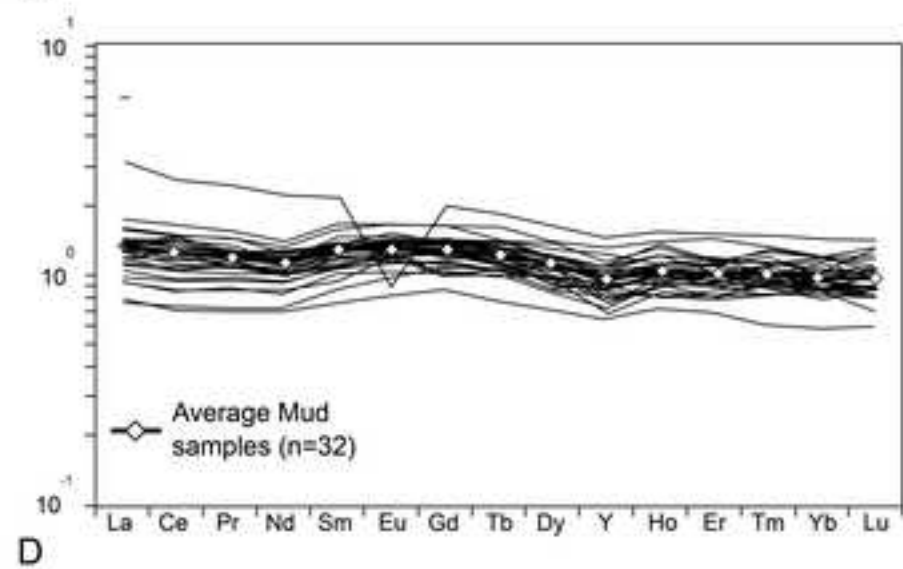
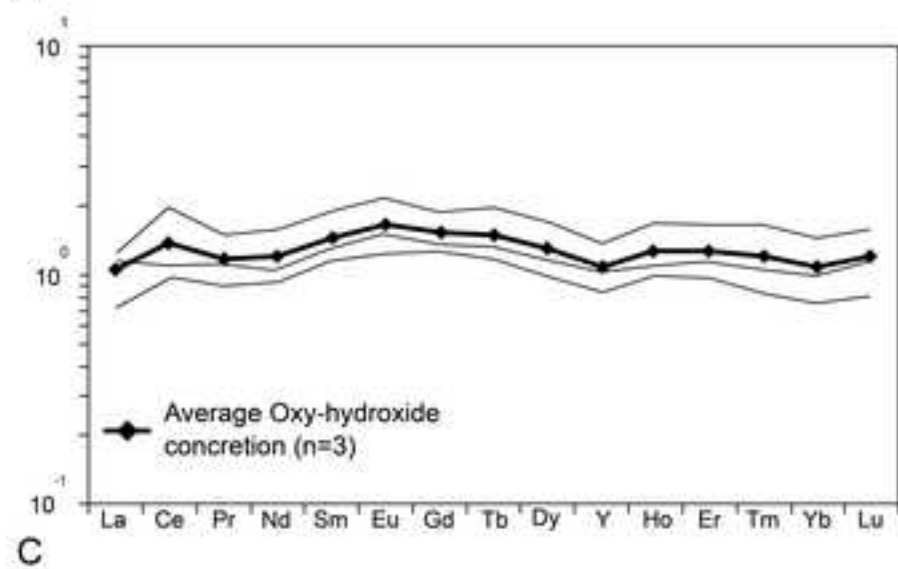
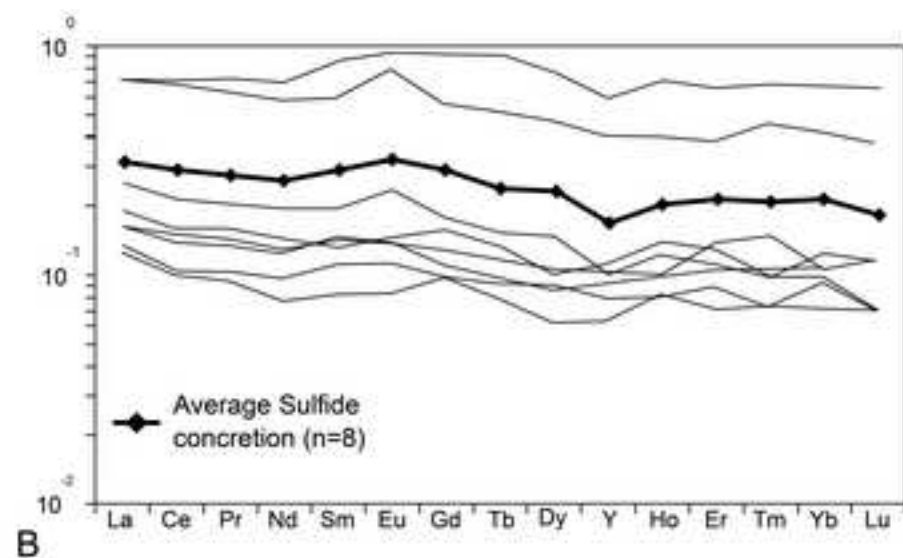
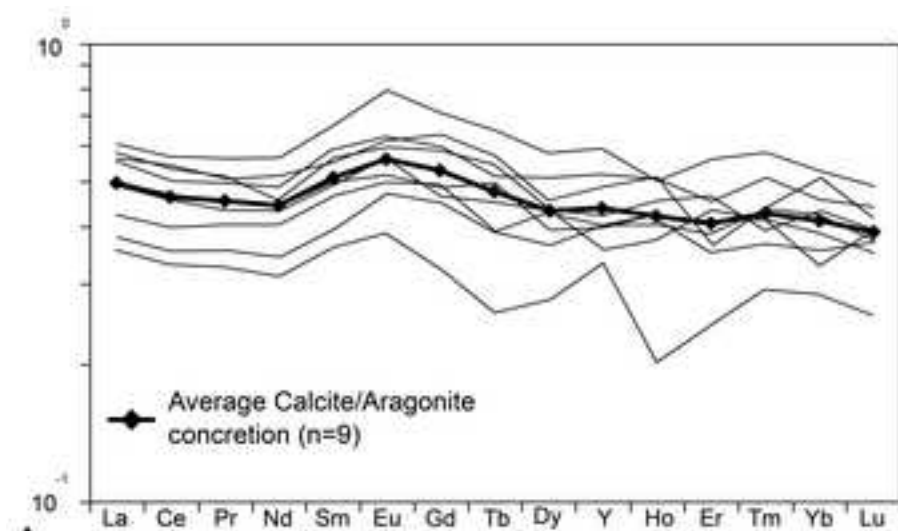


Figure 8
[Click here to download high resolution image](#)

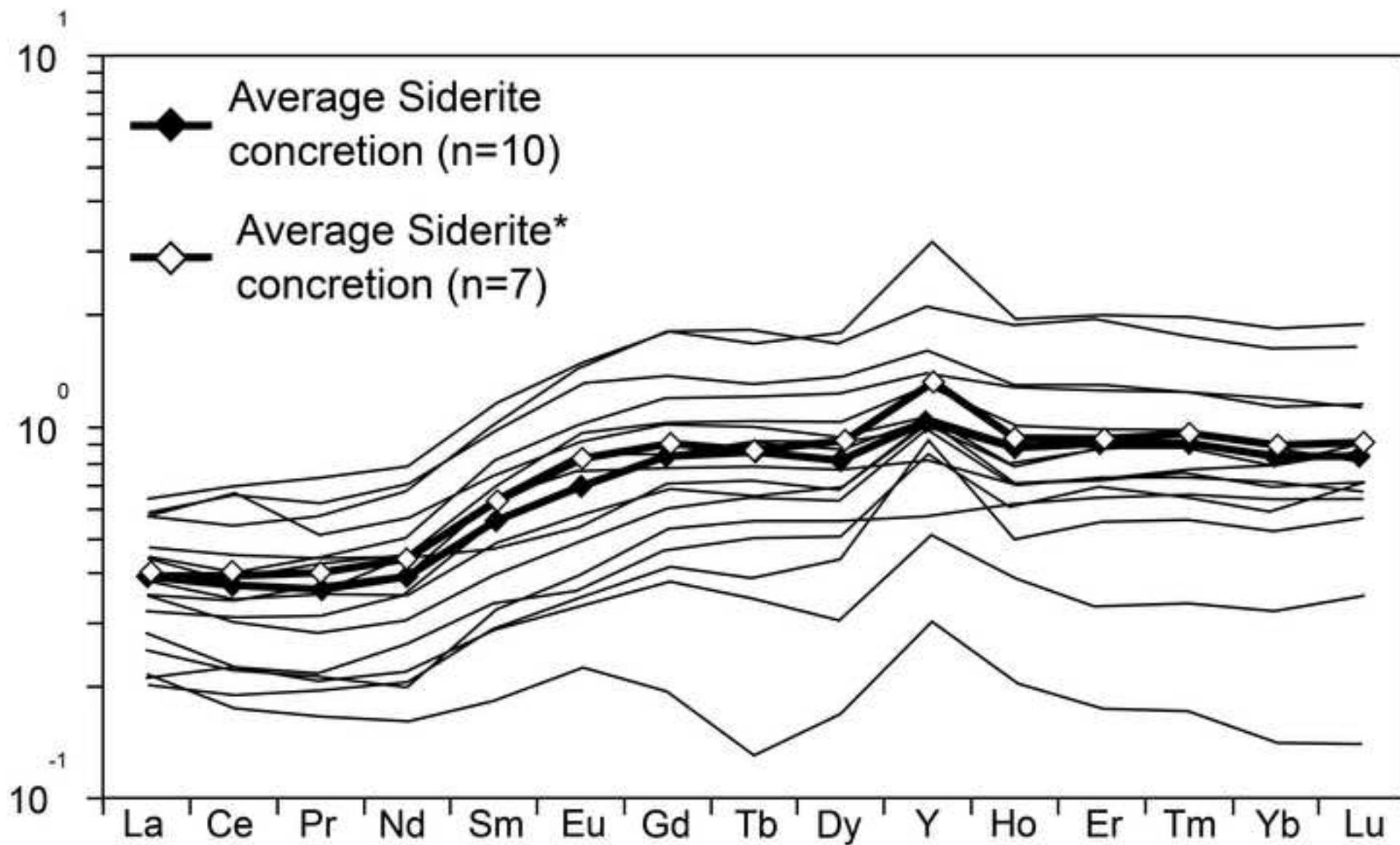


Fig. 8

Figure 9
[Click here to download high resolution image](#)

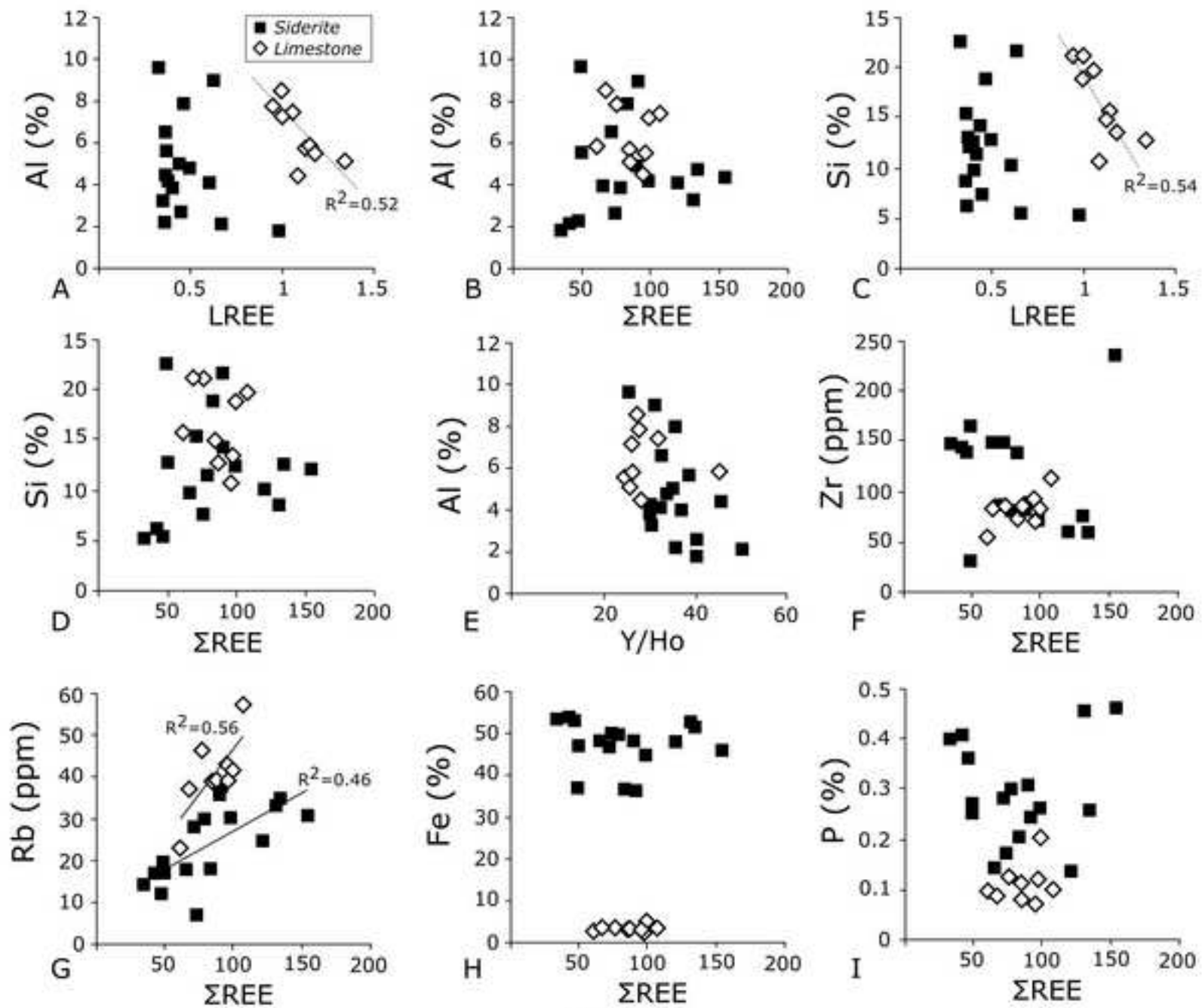


Fig. 9

Figure 10

[Click here to download high resolution image](#)

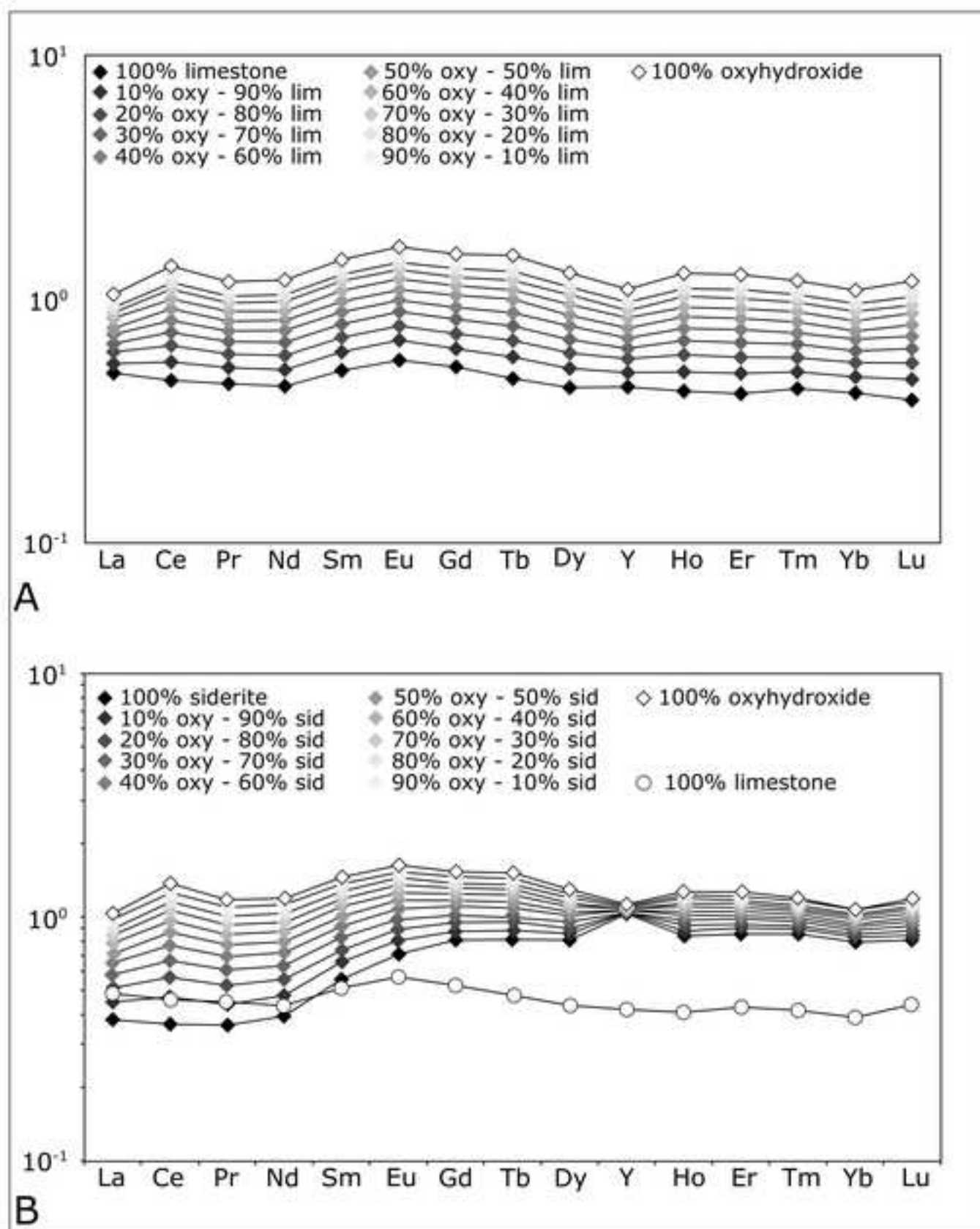


Fig. 10

Table 1

TABLE 1

Site	Sampling Station	Sample	Mineralogy				$\delta^{13}\text{C}$ (‰)	$\delta^{18}\text{O}$ (‰)	Depth below seafloor (m)
			Calcite (vol.%)	Dolomite (vol.%)	Aragonite (vol.%)	Other			
1	MB14_ROS05	Water						0	
	MVP11_GC36	Cal-V	-	-	-	Siderite (ter.)	10.4	9.5	6
	MVP11_GC26	Cal-T	-	-	-	Goethite			0.5
		Cal-I	-	-	-	Siderite (Qz)	10.6	9.2	5
2	MB14_ROS06	Water						0	
		Cal-L	-	-	-	Pyrite			0.5
	MVP11_BC25	Cal-Q	-	-	-	Pyrite			0.5
		Cal-Q1	-	-	-	Sulfur			0.5
		Cal-20	-	-	-	Siliciclastic			0.3
		Cal-21	-	-	-	Siliciclastic			0.8
		Cal-4	Trace	-	-	Siliciclastic			0.9
	MVP11_GC28	Cal-14	-	-	-	Pyrite			1.1
		Cal-18	-	-	-	Hematite			1.4
		Cal-12	-	-	-	Hematite			1.8
3	MB14_ROS07	Water						0	
		Cal-U	-	-	-	Siderite (ter.)	10.3	9.3	2
		Cal-S	-	-	-	Pyrite			3.5
	MVP11_GC29	Cal-Z	-	-	-	Pyrite			4
		Cal-W	-	-	-	Pyrite			4.1
		Cal-X	-	-	-	Pyrite			5
		Cal-Y	-	-	-	Pyrite			5
	MB14_BC05	Gas						0	
4	MVP11_GC12	Cal-G	-	-	-	Siderite (Qz)	8.4	9.5	6
	MB14_GC03	Cal-MB4	-	-	-	Siderite (Qz)			6.2
5		Cal-16	Trace			Siliciclastic			0.3
	MVP11_GC08	Cal-9	Trace			Siliciclastic			0.7
		Cal-15	Trace			Siliciclastic			3.6
		Cal-10	Trace			Siliciclastic			3.7
6	MB14_ROS08	Water						0	
	MVP11_BC02	Cal-D	-	-	-	Pyrite			0.2
	MB14_BC09	Gas						0	
		Cal-RR	-	-	-	Siderite (Qz)	8.7	9.3	0.3
	MVP11_GC03	Cal-31	-	-	-	Siliciclastic			0.4
		Cal-EE	-	-	-	Siderite (Qz)	9.1	9.1	1.3
		Cal-28	-	-	-	Siliciclastic			2.1
7	MB14_ROS09	Water						0	
		Cal-E	-	-	-	Siderite (ter.)	8.3	9.6	0-1
		Cal-R	Trace			Siderite (ter.)	7.7	9.9	0-1
		Cal-7	-	-	-	Siliciclastic			0-1
		Cal-8	-	-	-	Siliciclastic			0-1
	MVP11_GC17	Cal-1	-	-	-	Hematite			1.3
		Cal-2	-	-	-	Siliciclastic			3.2
		Cal-19	-	-	-	Siliciclastic			4
		Cal-6	Trace			Siliciclastic			4.8
		Cal-23	-	-	-	Siliciclastic			5.3
		Cal-A	-	-	-	Siderite (Qz)	8.7	8.7	6
	MVP11_BC01	Cal-K	-	-	-	Pyrite			0.5
		Cal-O	-	-	-	Pyrite			0.5
8	MB14_BC11	Water						0	
9		Cal-24	-	-	-	Siliciclastic			0.5
		Cal-5	-	-	-	Siliciclastic			1.5
	MVP11_GC07	Cal-13	-	-	-	Siliciclastic			2.5
		Cal-26	-	-	-	Siliciclastic			3.5
		Cal-3	-	-	-	Siliciclastic			3.8
		Cal-25	-	-	-	Siliciclastic			4.7
		Cal-11	-	-	-	Hematite			5.5
10	MVP11_BC04	Cal-P	-	-	-	Goethite			0.5
		Cal-F	-	-	-	Goethite			0.5
11	MVP11_GC10	Cal-M	-	-	-	Siderite (Qz)	-3.2	8.8	5
12	MVP11_GC15	Cal-27	Trace	-	-	Siliciclastic			3.6
		Cal-30	Trace	-	-	Siliciclastic			3.7
13		Cal-N	27.0	1.7	38.3		-35.8	4.7	0
	MVP11_GC16	Cal-N*	0.0	100.0	0.0		-9.9	1.4	0

Table 2

Table 2

Sample	Cal-B	Cal-C	Cal-N	Cal-H	Cal-BB	Cal-CC	Cal-AA	Cal-NN
Na ₂ O	0.38	0.43	0.45	0.54	0.56	0.81	0.58	0.48
MgO	2.73	3.27	3.00	1.93	2.05	1.80	2.03	1.47
Al ₂ O ₃	5.74	5.07	7.20	5.56	7.44	7.79	4.40	5.87
SiO ₂	14.87	12.73	18.80	13.57	19.67	21.22	10.73	15.72
P ₂ O ₅	0.08	0.11	0.20	0.12	0.10	0.12	0.07	0.09
K ₂ O	1.14	0.92	1.45	1.00	1.45	1.53	0.79	1.13
CaO	39.65	39.73	34.73	41.15	36.37	29.42	43.16	40.52
TiO ₂	0.35	0.29	0.46	0.29	0.49	0.43	0.28	0.28
MnO	0.06	0.10	0.06	0.03	0.05	0.06	0.04	0.05
Fe ₂ O ₃	3.05	3.09	4.84	2.17	3.28	3.24	2.34	2.70
L.O.I	31.04	33.76	27.90	32.66	26.97	32.11	34.40	30.63
TOT	99.08	99.50	99.08	99.02	98.42	98.52	98.83	98.94
La	19.0	18.8	21.6	22.2	16.2	23.0	13.6	14.5
Ce	36.5	37.7	43.1	42.6	31.7	45.3	26.3	28.2
Pr	3.9	3.9	4.5	4.5	3.6	5.0	2.9	3.1
Nd	14.7	14.9	17.6	15.5	13.7	19.2	10.6	11.6
Sm	2.7	2.8	3.1	3.1	2.6	3.7	2.0	2.2
Eu	0.6	0.6	0.7	0.6	0.5	0.9	0.4	0.5
Gd	2.2	2.3	3.0	2.7	2.3	3.3	1.5	2.1
Tb	0.4	0.4	0.4	0.4	0.3	0.5	0.2	0.3
Dy	2.0	1.9	2.1	2.1	2.0	2.7	1.3	1.7
Ho	0.4	0.4	0.5	0.5	0.4	0.5	0.2	0.4
Er	1.2	1.2	1.0	1.3	1.1	1.6	0.7	1.0
Tm	0.2	0.2	0.2	0.2	0.2	0.2	0.1	0.2
Yb	1.1	0.9	1.4	1.2	1.2	1.5	0.8	1.0
Lu	0.2	0.2	0.2	0.2	0.2	0.2	0.1	0.2
ΣREE	85.0	86.0	99.4	97.2	76.0	107.6	60.7	67.0
Y/Ho	25.9	25.7	26.1	25.3	27.5	32.0	45.0	27.5
Ce/Ce*	1.04	1.05	1.08	0.93	0.98	1.01	0.98	0.96
Eu/Eu*	1.18	1.04	1.11	1.06	1.13	1.20	1.20	1.20
Gd/Gd*	1.00	0.98	1.13	1.06	1.19	1.08	1.11	1.15
Pr _{SN} /Yb _{SN}	1.13	1.35	1.00	1.19	0.95	1.06	1.15	1.00

Table 3**Table 3**

Sample	Cal-I	Cal-G	Cal-M	Cal-E	Cal-R	Cal-A	Cal-V	Cal-U
Na₂O	0.59	0.31	0.29	0.78	0.56	0.42	0.47	2.32
MgO	1.29	1.98	2.11	1.44	1.01	0.73	0.98	1.16
Al₂O₃	7.93	2.21	3.27	9.66	5.66	4.30	4.02	4.10
SiO₂	18.78	5.52	8.75	22.64	12.89	12.38	9.80	10.23
P₂O₅	0.20	0.36	0.46	0.26	0.27	0.26	0.14	0.14
K₂O	0.96	0.33	0.52	0.09	0.67	0.52	0.55	0.68
CaO	2.89	3.59	3.32	1.10	3.04	1.52	5.56	3.41
TiO₂	0.27	0.12	0.16	0.31	0.18	0.16	0.19	0.18
MnO	0.61	1.64	0.94	0.53	0.89	0.68	1.28	0.83
Fe₂O₃	36.85	53.33	53.01	37.24	47.12	44.79	48.65	48.22
L.O.I	28.77	30.36	26.87	22.74	26.98	33.65	27.92	26.18
TOT	99.15	99.75	99.69	96.78	99.24	99.41	99.56	97.43
La	16.9	10.7	8.2	16.7	21.5	9.7	13.7	18.1
Ce	31.8	18.0	18.0	33.0	43.0	18.0	24.0	36.0
Pr	3.2	1.9	2.0	4.0	5.1	1.9	2.5	4.0
Nd	14.6	7.5	9.1	17.3	22.9	6.9	10.2	15.4
Sm	2.6	1.6	1.9	4.6	5.7	1.8	2.2	3.6
Eu	0.6	0.4	0.4	1.1	1.6	0.4	0.5	0.8
Gd	3.2	1.8	2.2	5.6	8.5	2.5	2.8	3.6
Tb	0.6	0.3	0.4	1.0	1.4	0.4	0.5	0.6
Dy	3.2	1.4	2.5	5.7	7.9	2.6	3.0	3.6
Ho	0.8	0.4	0.6	1.3	1.9	0.6	0.7	0.7
Er	2.5	1.0	2.0	3.6	5.6	1.9	2.1	2.1
Tm	0.4	0.1	0.3	0.5	0.7	0.3	0.3	0.3
Yb	2.2	0.9	1.7	3.4	4.6	1.9	2.0	2.0
Lu	0.4	0.2	0.3	0.5	0.7	0.3	0.3	0.3
ΣREE	82.7	46.0	49.6	98.2	131.0	49.2	64.9	91.1
Y/Ho	35.4	35.1	38.4	30.2	30.2	25.6	37.1	31.4
Ce/Ce*	1.3	1.1	1.2	1.0	1.1	1.0	1.1	1.0
Eu/Eu*	1.0	1.1	0.9	1.1	1.2	1.0	1.1	1.1
Gd/Gd*	1.1	1.2	1.1	1.1	1.2	1.1	1.1	1.1
Pr_{SN}/Yb_{SN}	0.5	0.7	0.4	0.4	0.4	0.3	0.4	0.6

Table 4

Table 4

Sample	Cal-D	Cal-O	Cal-L	Cal-Q	Cal-S	Cal-Z	Cal-W	Cal-X
Na ₂ O	0.62	1.58	0.08	0.53	0.38	0.90	0.55	1.66
MgO	0.52	0.72	0.65	0.44	0.28	0.53	0.95	0.76
Al ₂ O ₃	5.14	4.54	5.39	3.77	3.13	6.42	12.30	20.38
SiO ₂	12.02	10.79	14.50	9.55	7.47	14.83	29.48	33.78
P ₂ O ₅	0.09	0.10	0.23	0.04	0.00	0.05	0.13	0.19
K ₂ O	0.91	1.44	1.12	0.60	0.55	0.98	2.39	1.91
CaO	0.41	1.14	0.43	0.21	0.18	0.36	0.74	3.20
TiO ₂	0.19	0.13	0.24	0.14	0.12	0.23	0.57	0.98
MnO	0.02	0.02	0.03	0.03	0.03	0.05	0.03	0.06
Fe ₂ O ₃	30.79	29.38	10.74	28.07	31.19	26.08	13.13	10.55
L.O.I	33.8	30.2	44.9	37.0	36.2	32.1	29.1	15.0
TOT	84.5	80.0	78.3	80.3	79.5	82.5	89.4	88.4
La	5.1	9.5	7.3	4.8	6.2	6.3	27.5	26.9
Ce	8.4	17.2	12.9	8.0	11.0	12.2	54.4	55.9
Pr	0.9	1.8	1.4	0.8	1.2	1.3	5.6	6.3
Nd	3.2	6.6	4.8	2.6	4.2	4.4	19.6	23.9
Sm	0.6	1.1	0.8	0.5	0.8	0.8	3.3	4.8
Eu	0.1	0.3	0.2	0.1	0.2	0.2	0.9	1.0
Gd	0.5	0.8	0.7	0.5	0.5	0.6	2.6	4.3
Tb	0.1	0.1	0.1	0.1	<0.1	<0.1	0.4	0.7
Dy	0.4	0.7	0.5	0.3	0.4	0.5	2.2	3.6
Ho	0.1	0.1	0.1	0.1	<0.1	0.1	0.4	0.7
Er	0.3	0.3	0.4	0.2	0.3	0.4	1.1	1.9
Tm	0.0	0.0	0.0	0.0	<0.05	0.1	0.2	0.3
Yb	0.3	0.3	0.4	0.2	0.3	0.3	1.2	1.9
Lu	0.0	0.0	0.1	0.0	<0.04	0.1	0.2	0.3
ΣREE	20.0	38.9	29.6	18.1	25.0	27.2	119.5	132.5
Y/Ho	26.3	22.5	21.4	21.3	0.0	0.0	27.5	22.9
Ce/Ce*	0.9	1.0	0.9	0.9	1.0	0.9	1.0	1.0
Eu/Eu*	1.1	1.3	1.1	1.0	1.1	1.1	1.4	1.1
Gd/Gd*	1.0	1.1	1.2	1.2	0.9	1.1	1.0	1.0
Pr _{SN} /Yb _{SN}	1.1	2.1	1.3	1.3	1.2	1.4	1.5	1.1

Table 5**Table 5**

Sample	Cal-F	Cal-P	Cal-T
Na₂O	0.27	0.07	7.77
MgO	1.11	1.85	1.18
Al₂O₃	9.93	16.51	9.24
SiO₂	20.25	36.12	25.14
P₂O₅	1.96	2.81	0.38
K₂O	1.35	2.50	2.19
CaO	0.48	1.23	0.92
TiO₂	0.38	0.79	0.64
MnO	0.04	0.41	0.08
Fe₂O₃	52.09	24.27	13.51
L.O.I	10.5	7.3	6.5
TOT	98.3	93.9	67.5
La	27.6	48.1	43.8
Ce	77.4	159.6	87.8
Pr	7.9	13.5	9.8
Nd	32.4	53.5	35.5
Sm	6.4	10.5	7.3
Eu	1.3	2.3	1.6
Gd	5.9	9.0	6.4
Tb	0.9	1.5	1.0
Dy	4.6	7.9	5.6
Ho	1.0	1.7	1.1
Er	2.7	4.8	3.3
Tm	0.3	0.7	0.4
Yb	2.1	4.2	2.9
Lu	0.4	0.7	0.5
ΣREE	171.0	318.0	207.0
Y/Ho	22.5	22.2	25.6
Ce/Ce*	1.2	1.4	0.9
Eu/Eu*	1.1	1.1	1.1
Gd/Gd*	1.1	1.0	1.0
Pr_{SN}/Yb_{SN}	1.2	1.0	1.1

Table 6

Table 6																
Sample	Cal-1	Cal-2	Cal-3	Cal-4	Cal-5	Cal-6	Cal-7	Cal-8	Cal-9	Cal-10	Cal-11	Cal-12	Cal-13	Cal-14	Cal-15	Cal-16
Na ₂ O	0.2	9.0	0.0	0.2	4.3	8.5	3.0	0.0	0.3	0.0	6.7	0.0	0.0	1.2	6.9	0.0
MgO	2.0	0.4	1.9	0.9	1.4	0.6	1.1	1.4	2.1	2.3	1.2	1.1	2.3	0.3	1.9	2.3
Al ₂ O ₃	20.8	6.2	19.8	23.1	16.1	8.2	11.8	15.3	15.2	17.7	13.5	20.6	20.1	10.3	10.7	18.1
SiO ₂	52.5	16.8	51.3	54.5	39.9	21.5	28.5	38.7	41.0	46.8	34.4	53.3	52.5	31.6	27.6	44.9
P ₂ O ₅	0.2	0.1	0.2	0.2	0.1	0.1	0.2	0.2	0.2	0.2	0.1	0.2	0.2	0.1	0.1	0.4
K ₂ O	3.7	1.8	3.7	4.1	3.2	2.3	2.0	2.9	3.3	3.3	2.9	3.1	3.8	3.4	2.5	3.5
CaO	1.5	0.9	1.1	1.9	1.2	0.7	1.6	1.2	7.7	8.8	1.2	0.9	2.8	0.8	5.3	5.6
TiO ₂	1.2	0.8	1.2	1.3	1.1	0.9	0.5	0.9	0.9	1.0	1.0	1.0	1.2	0.3	0.8	1.0
MnO	0.1	0.1	0.0	0.0	0.0	0.1	0.5	0.0	0.1	0.1	0.1	0.0	0.1	0.1	0.1	0.1
Fe ₂ O ₃	7.1	6.0	7.3	3.6	5.9	5.6	24.4	6.1	8.0	7.0	6.4	4.9	7.3	12.7	6.1	11.7
L.O.I	6.6	5.8	6.8	6.6	6.4	6.4	17.2	8.4	10.8	10.0	6.7	9.6	7.2	19.9	11.2	9.6
TOT	95.8	47.8	93.2	96.4	79.8	54.7	90.7	75.2	89.6	97.3	74.3	94.6	97.4	80.6	73.1	97.0
La	50.8	54.4	54.1	53.2	52.1	60.4	29.6	51.0	41.7	47.8	54.2	53.9	51.1	116.7	44.5	48.7
Ce	101.6	105.8	105.7	96.9	101.4	118.7	58.8	100.7	83.1	87.9	104.9	112.3	98.0	204.9	83.3	91.9
Pr	10.9	11.5	11.1	9.7	10.7	12.8	6.5	10.9	8.9	9.6	11.2	11.7	10.9	21.5	9.6	9.9
Nd	41.5	38.7	42.5	35.2	39.6	45.7	24.6	41.2	34.1	36.4	43.2	38.2	41.6	74.9	33.7	34.4
Sm	7.3	7.6	7.4	6.2	7.5	8.7	4.9	7.2	5.9	6.5	7.4	7.5	7.5	11.8	6.6	6.2
Eu	1.5	1.7	1.5	1.4	1.5	1.8	1.1	1.5	1.2	1.3	1.5	1.3	1.5	1.0	1.3	1.3
Gd	6.2	6.5	6.5	4.8	6.4	7.8	5.1	6.0	5.3	5.7	6.6	5.6	6.2	9.2	5.7	5.6
Tb	1.0	1.0	1.0	0.8	1.0	1.3	0.8	0.9	0.8	0.9	1.0	0.9	1.0	1.4	0.8	0.8
Dy	4.9	5.7	5.7	4.0	5.4	6.6	5.0	4.4	4.5	4.5	5.1	4.4	5.1	7.5	4.3	4.9
Ho	1.1	1.2	1.2	0.9	1.1	1.4	1.0	1.0	1.0	0.9	1.1	0.8	1.0	1.5	1.0	1.0
Er	3.3	3.4	3.5	2.6	3.4	4.1	3.0	2.8	2.6	2.8	3.1	2.3	3.1	4.3	2.6	2.7
Tm	0.4	0.5	0.5	0.3	0.4	0.6	0.4	0.4	0.4	0.4	0.4	0.4	0.4	0.6	0.4	0.4
Yb	2.8	3.1	3.4	2.5	2.9	3.5	2.6	2.5	2.4	2.5	3.1	2.6	2.9	4.0	2.6	2.2
Lu	0.4	0.4	0.5	0.4	0.4	0.6	0.4	0.4	0.4	0.4	0.4	0.4	0.5	0.6	0.4	0.4
ΣREE	233.8	241.5	244.5	218.7	234.0	273.8	143.7	231.0	192.1	207.4	243.2	242.1	230.8	459.8	196.9	210.4
Y/Ho	23.8	23.8	24.9	21.8	22.8	25.7	28.2	23.2	23.6	27.1	25.6	22.3	26.3	26.3	23.8	23.7
Ce/Ce*	1.0	0.9	1.1	1.1	1.0	1.0	1.0	1.0	1.0	1.0	1.1	0.9	1.0	1.0	0.9	0.9
Eu/Eu*	1.1	1.1	1.1	1.2	1.1	1.0	1.0	1.1	1.1	1.0	1.0	0.9	1.1	0.4	1.0	1.1

Table 7

Sampling station	CO ₂ (%)	N ₂ (%)	O ₂ (%)	Ar (%)	CH ₄ (%)	δ ¹³ C _{CO₂} (‰)	δ ¹⁸ O _{CO₂} (‰)
MB14 BC05	98.73	1.08	0.11	0.026	0.056	-1.1	-4.4
MB14 BC09	98.61	1.26	0.053	0.031	0.051	-1.8	-2.4

Table 8

	Alk.	F ⁻	Cl ⁻	Br ⁻	NO ₃ ⁻	SO ₄ ²⁻	Ca ²⁺	Mg ²⁺
MB14_ROS05	232	1.95	23606	61	11.5	3876	482	1512
MB14_ROS06	232	1.20	23413	79	n.d.	3901	507	1527
MB14_ROS07	231	2.32	23639	72	n.d.	3920	506	1494
MB14_ROS08	159	2.52	23323	74	9.0	3918	521	1482
MB14_ROS09	243	n.d.	23132	70	20.1	3824	486	1499

Alk.: total alkalinity

n.d.: not determined

Supplementary Material S1

[Click here to download Supplementary Material \(for online publication only\): Supplementary Material 1.xls](#)